# Inhibitory G proteins play multiple roles to polarize sensory hair cell morphogenesis

Amandine Jarysta[1], Abigail L.D. Tadenev[1], Matthew Day[1], Barry Krawchuk[1], Benjamin E. Low[1], Michael V. Wiles[1], and Basile Tarchini[1,2 #]

[1]The Jackson Laboratory, Bar Harbor, ME 04609, USA. [2]Tufts University School of Medicine, Boston, MA 02111, USA.

[#]Corresponding author: basile.tarchini@jax.org

## ABSTRACT

Inhibitory G alpha (GNAI or Gαi) proteins are critical for the polarized morphogenesis of sensory hair cells and for hearing. The extent and nature of their actual contributions remains unclear, however, as previous studies did not investigate all GNAI proteins and included non-physiological approaches. Pertussis toxin can downregulate functionally redundant GNAI1, GNAI2, GNAI3 and GNAO proteins, but may also induce unrelated defects. Here we directly and systematically determine the role(s) of each individual GNAI protein in mouse auditory hair cells. GNAI2 and GNAI3 are similarly polarized at the hair cell apex with their binding partner GPSM2, whereas GNAI1 and GNAO are not detected. In *Gnai3* mutants, GNAI2 progressively fails to fully occupy the subcellular compartments where GNAI3 is missing. In contrast, GNAI3 can fully compensate for the loss of GNAI2 and is essential for hair bundle morphogenesis and auditory function. Simultaneous inactivation of *Gnai2* and *Gnai3* recapitulates for the first time two distinct types of defects only observed so far with pertussis toxin: 1) a delay or failure of the basal body to migrate off-center in prospective hair cells, and 2) a reversal in the orientation of some hair cell types. We conclude that GNAI proteins are critical for hair cells to break planar symmetry and to orient properly before GNAI2/3 regulate hair bundle morphogenesis with GPSM2.

## INTRODUCTION

Developing sensory hair cells (HC) in the inner ear undergo a complex polarization process to detect and interpret mechanical stimuli, including sound. Each mature HC is able to detect stimuli in a directional manner by developing an asymmetric brush of actin-based membrane protrusions, or stereocilia: the hair bundle. Neighboring HC also adopt concerted orientations to align their hair bundles, a property known as planar cell polarity (PCP). One subclass of heterotrimeric guanine nucleotide-binding (G) protein was intimately associated with different levels of mouse HC polarization: inhibitory G alpha subunits (GNAI1, GNAI2, GNAI3 and GNAO; collectively GNAI or G$\alpha$i) (Figure 1A). However, several roles proposed for GNAI proteins have not been validated physiologically, and the individual contribution of each GNAI remains uncertain.

HC polarization along the epithelial plane starts with the off-center migration of the basal body and its associated primary cilium, the kinocilium (Denman-Johnson & Forge, 1999; Mbiene & Sans, 1986; Tilney et al, 1992). At that stage, Regulator of G protein Signaling 12 (RGS12) is required for GNAI and the G protein signaling modulator 2 (GPSM2) scaffold to form a polarized complex at the apical membrane on the side of the off-center basal body (Akturk et al, 2022; Ezan et al, 2013; Tarchini et al, 2013). GPSM2-GNAI is best known as a highly conserved protein complex orienting the mitotic spindle during progenitor divisions (Du et al, 2001; Schaefer et al, 2001; Schaefer et al, 2000; Woodard et al, 2010). In post-mitotic HC, GPSM2-GNAI first excludes microvilli and microvilli-derived stereocilia from the portion of the HC surface where it resides, the expanding bare zone (Figure 1B). Bare zone expansion then pushes back the basal body/kinocilium from a more eccentric position near the lateral junction to a less eccentric position at the vertex of the forming hair bundle. Later, GPSM2-GNAI becomes enriched at the distal tip of row 1 stereocilia abutting the bare zone (Tarchini et al, 2016). In these stereocilia, GPSM2-GNAI is a module of the elongation complex that also comprises MYO15A, WHRN and EPS8 (Mauriac et al, 2017; Tadenev et al, 2019). GPSM2-GNAI is required at row 1 tips for boosting enrichment of other elongation complex partners, and presumably actin incorporation, compared to further stereocilia rows. GPSM2-GNAI thus

79 confers row 1 its tallest identity and the hair bundle its asymmetric graded-height
80 morphology.
81
82 Pertussis toxin (ptx) has been extensively used as a tool to ADP-ribosylate the GNAI
83 subunit and dissociate heterotrimeric Gαiβγ protein complexes from G protein-coupled
84 receptors (GPCR) to inactivate downstream signaling (Locht et al, 2011). *In vivo*
85 expression of ptx catalytic subunit (ptx-S1 or ptxA) prevents normal enrichment and
86 polarization of GPSM2-GNAI in developing HC (Tadenev et al, 2019; Tarchini et al, 2013),
87 suggesting that ADP-ribosylation directly or indirectly inhibits GPSM2-GNAI function as
88 well. Ptx provokes immature-looking hair bundles with severely stunted stereocilia,
89 mimicking defects in *Gpsm2* mutants and *Gnai2; Gnai3* double mutants (Beer-Hammer
90 et al, 2018; Mauriac et al, 2017; Tadenev et al, 2019; Tarchini et al, 2016). In contrast,
91 stereocilia height is more variably reduced in *Gnai3* single mutants, with defects more
92 severe at the cochlear base (Beer-Hammer et al, 2018; Mauriac et al, 2017). This can
93 explain why hearing loss is more severe at high frequencies in *Gnai3* mutants, but
94 profound at all frequencies in a *ptxA* model and in mutants lacking GPSM2 or both GNAI2
95 and GNAI3 (Beer-Hammer et al, 2018; Mauriac et al, 2017; Tarchini et al, 2016).
96 Surprisingly, before affecting hair bundle differentiation at postnatal stages, ptx also
97 causes two distinct defects in HC polarization at embryonic stages.
98
99 First, one study reported that a high dose of ptx in cultured explants of the developing
100 cochlea results in a low proportion of symmetrical HC with a central kinocilium surrounded
101 by a rounded hair bundle (Figure 1C) (Ezan et al, 2013). Because GPSM2-GNAI recruits
102 partners to pull on astral microtubules during mitotic spindle orientation, the authors
103 proposed that GPSM2-GNAI functions similarly and triggers the basal body off-center
104 migration when post-mitotic HC break planar symmetry. However, this hypothesis has not
105 been validated *in vivo* to date. Studies where *Gpsm2* (Bhonker et al, 2016; Ezan et al,
106 2013; Mauriac et al, 2017; Tarchini et al, 2013), *Gnai3* (Beer-Hammer et al, 2018; Ezan
107 et al, 2013; Mauriac et al, 2017) or *Gnai2; Gnai3* (Beer-Hammer et al, 2018) were
108 inactivated did not report symmetrical HC. In addition, mouse strains expressing ptxA *in*

*vivo* also did not produce symmetrical cochlear HC (Tarchini et al, 2013; Tarchini et al, 2016).

Second, ptx experiments induced striking HC misorientation. In the cochlea, misorientation manifested as a 180° inversion of outer HC in the first and second row (OHC1-2) whereas inner HC (IHC) and OHC3 were much less affected (Figure 1C) (Ezan et al, 2013; Kindt et al, 2021; Tarchini et al, 2013). In the vestibular system, ptxA expression abrogated the line of polarity reversal and thus the mirror-image HC organization characteristic of macular organs, the utricle and saccule (Jiang et al, 2017; Kindt et al, 2021). Normal orientation reversal was also lost upon inactivating two endogenous mouse proteins: the transcription factor EMX2 in the maculae (Jiang et al, 2017) and the orphan GPCR GPR156 in cochlear OHC1-2 and in the maculae (Kindt et al, 2021). Together, these recent studies uncovered an EMX2>GPR156>GNAI signaling cascade that secures a normal pattern of HC orientation by reversing *Emx2*-positive HC. GNAI signals downstream of GPR156 to reverse the orientation of the basal body migration in *Emx2*-positive compared to *Emx2*-negative HC (Tona & Wu, 2020) (reviewed in (Tarchini, 2021)). While ptx impact on orientation thus appears to be physiologically relevant, HC misorientation was surprisingly not reported in single *Gnai3* or double *Gnai2; Gnai3* mutants (Beer-Hammer et al, 2018; Mauriac et al, 2017).

In summary, the importance of the GPSM2-GNAI complex for hair bundle development is well-established, but multiple discrepancies cast a doubt on whether GNAI proteins also assume earlier polarization roles. Specific questions include whether GNAI proteins participate in the mechanism that pushes the basal body away from the cell center, and in the distinct EMX2>GPR156 mechanism that makes a binary decision on the direction of this push (Figure 1B). Furthermore, it remains unclear whether GNAI2 and GNAI3 adopt similar or distinct distributions in HC, and whether GNAI1 or GNAO also participate in these processes.

In this study, we embarked on a systematic analysis of single and combined *Gnai1*, *Gnai2*, *Gnai3* and *Gnao1* mouse mutants to solve the actual role(s) of GNAI/O proteins

during HC differentiation. Our results confirm that GNAI3 is the only GNAI/O protein required for normal hair bundle morphogenesis and normal auditory brainstem response (ABR) thresholds. In absence of GNAI3, GNAI2 can fully compensate at embryonic stages but is not enriched with GPSM2 long enough to ensure normal hair bundle morphogenesis at postnatal stages. We directly demonstrate that GNAI proteins have two early polarization roles independent of GPSM2 during embryogenesis. In sum, GNAI function is instrumental for HC to a) break planar symmetry, b) adopt a proper binary orientation along the PCP axis downstream of EMX2 and GPR156, and c) elongate and organize stereocilia into a functional hair bundle with GPSM2.

150 **RESULTS**

151

152 **A near-comprehensive collection of *Gnai/o* mouse mutants**

153 In order to interrogate the individual and combined roles of all inhibitory G proteins during
154 HC differentiation, we obtained or generated mouse strains to build a collection of single
155 and double *Gnai/o* mutants. Single *Gnai1* and *Gnai3* mutants were derived from the
156 *Gnai1*$^{tm1Lbi}$*; Gnai3*$^{tm1Lbi}$ double mutant strain (hereafter *Gnai1*$^{neo}$*; Gnai3*$^{neo}$) (Jiang et al,
157 2002) by segregating individual mutations upon breeding (see Methods and Supp. Table
158 1 for details on all strains). We generated a new constitutive *Gnai2* mutant strain (*Gnai2*$^{del}$)
159 carrying a deletion of exons 2 to 4 (Figure 2 Supp. 1A; see Methods). Finally, we obtained
160 and derived two *Gnao1* mutant strains: a constitutive inactivation allele where a neomycin
161 cassette disrupts exon 6 (*Gnao1*$^{neo}$) (Jiang et al, 1998) and the conditional inactivation
162 allele *Gnao1*$^{tm1c(EUCOMM)Hmgu}$ (hereafter *Gnao1*$^{flox}$*)*. As simultaneous constitutive loss of
163 GNAI1 and GNAI2 was reported as viable (Plummer et al, 2012), we established a
164 *Gnai1*$^{neo}$; *Gnai2*$^{del}$ double mutant strain in addition to *Gnai1*$^{neo}$*; Gnai3*$^{neo}$ (Jiang et al,
165 2002). In contrast, double inactivation of *Gnai2; Gnai3* is lethal around Embryonic (E) day
166 10.5, before HC are born (Gohla et al, 2007). Consequently, we generated a new *Gnai3*$^{flox}$
167 strain by flanking exons 2 and 3 with *loxP* sites (Figure 2 Supp. 1B; see Methods). We
168 then generated conditional *FoxG1-Cre; Gnai2*$^{del}$*; Gnai3*$^{flox}$ double mutants where *Gnai3*
169 inactivation occurs as early as E8.5 in the otic vesicle (Hebert & McConnell, 2000).
170 Investigating all *Gnai/o* strains in the same genetic background was unrealistic for
171 feasibility and lethality reasons. We reasoned that apical HC development is probably
172 highly constrained and less likely to be influenced by genetic heterogeneity compared to
173 susceptibility to disease, for example.

174

175 As two of the three defects directly attributed to GNAI/O dysfunction were only observed
176 using pertussis toxin (Figure 1C), the *Gnai/o* strains above needed to be compared to a
177 strain expressing ptxA in HC. We used our *R26*$^{LSL\text{-}myc:ptxA}$ strain (hereafter *LSL-myc:ptxA*)
178 expressing N-terminal myc-tagged ptxA upon Cre recombination (Figure 2 Supp. 1C)
179 (Tarchini et al, 2016). Because a related *R26*$^{LSL\text{-}ptxAa:myc}$ strain carrying a C-terminal myc
180 tag (Regard et al, 2007) caused milder HC misorientation defects than *LSL-myc:ptxA* in

181 the vestibular system (Jiang et al, 2017; Kindt et al, 2021), we wondered whether the myc
182 tag could weaken toxin activity even perhaps when located N-terminal. Consequently, we
183 generated a new strain, *R26*$^{DIO\text{-}ptxA}$ (hereafter *DIO-ptxA*), where untagged ptxA is flanked
184 by double-inverted *lox* sites and flipped from the non-coding to the coding strand upon
185 Cre recombination (Figure 2 Supp. 1D; see Methods) (Schnutgen et al, 2003). In *DIO-*
186 *ptxA, ptxA* expression is driven by a strong artificial CAG promoter, and not by the
187 endogenous *R26* promoter as in previous strains (Regard et al, 2007; Tarchini et al,
188 2016). We bred *LSL-myc:ptxA* and *DIO-ptxA* either with *FoxG1*-Cre active in otic
189 progenitors (Hebert & McConnell, 2000), or alternatively with *Atoh1-Cre* (Matei et al,
190 2005) to limit GNAI/O inhibition to post-mitotic HC. Supplementary Table 1 summarizes
191 the strains used in this study, their origin, genetic background and viability.
192
193 **Only GNAI3 is required for hair bundle morphogenesis yet GNAI2 participates**
194 To investigate the role of individual GNAI/O proteins in HC development, we imaged hair
195 bundles in 3-week-old mutant and control littermate mice at the mid-cochlear position
196 using scanning electron microscopy (SEM). Single *Gnai1* or *Gnai2* mutants as well as
197 double *Gnai1; Gnai2* mutants did not show overt defects in OHC or IHC (Figure 2A). In
198 single *Gnai3* mutants by contrast, some OHC hair bundles appeared truncated, and IHC
199 displayed variably shortened row 1 stereocilia as well as supernumerary stereocilia rows
200 (Figure 2A-B), as previously described (Mauriac et al, 2017). The same defects were
201 observed in double *Gnai1; Gnai3* mutants and, as reported previously, in the *LSL-*
202 *myc:ptxA* model (Figure 2A-B) (Tadenev et al, 2019). A constitutive (*Gnao1*$^{neo}$) or
203 conditional (*Atoh1-Cre; Gnao1*$^{flox}$*)* inactivation of *Gnao1* did not produce overt apical HC
204 defects (Figure 2 Supp. 1E-F). Conditional inactivation of *Gnao1* also did not enhance
205 defects in the *Gnai1; Gnai3* mutant background (Figure 2 Supp. 1F).
206
207 In addition, *myc:ptxA* expression inverted the orientation of OHC1-2s (Figure 2A), as
208 expected since ptxA inactivates the EMX2>GPR156>GNAI signaling cascade that
209 defines HC orientation along the PCP axis (Kindt et al, 2021; Tarchini et al, 2013; Tarchini
210 et al, 2016). However, a defect in HC orientation was not observed in single *Gnai1*, *Gnai2*,
211 *Gnai3* mutants, or in double *Gnai1*; *Gnai2* and *Gnai1*; *Gnai3* mutants (Figure 2A). Despite

212 extensive breeding, we could only obtain one adult animal carrying a double *Gnai2; Gnai3*
213 inactivation due to postnatal lethality (*FoxG1-Cre; Gnai2*$^{del/del}$*; Gnai3*$^{flox/flox}$; see Supp.
214 Table 1). Remarkably, this unique specimen not only recapitulated stereocilia stunting
215 and extra stereocilia rows observed in the *Gnai3*$^{neo}$, *Gnai1*$^{neo}$*; Gnai3*$^{neo}$ and *LSL-myc:ptxA*
216 models (Figure 2A-B), but apparently also OHC1-2 misorientation only observed to date
217 in the *LSL-myc:ptxA* and *Gpr156* mutants (Figure 2A) (Kindt et al, 2021). This result
218 suggests that endogenous GNAI proteins are involved in HC orientation, and that GNAI2
219 can function in the EMX2>GPR156>GNAI signaling cascade to secure proper OHC1-2
220 orientation in *Gnai1; Gnai3* double mutants. This point is verified and expanded below
221 when neonate HC orientation is addressed.
222
223 To acquire a quantitative view of *Gnai* mutant defects and help comparisons, we first
224 focused on IHC and measured row 1 stereocilia height and width, as well as the number
225 of stereocilia in row 1 and the number of rows in the bundle in all strains (Figure 2C-F).
226 This analysis uncovered a *Gnai3*$^{neo}$ < *Gnai1*$^{neo}$*; Gnai3*$^{neo}$ < *LSL-myc:ptxA* < *FoxG1-Cre;*
227 *Gnai2*$^{del}$*; Gnai3*$^{flox}$ allelic series along which a) defects increased in severity, as
228 manifested by increased variability and decreased averages (row 1 height; Figure 2C),
229 and b) new defects appeared (excess row 1 stereocilia only observed in *LSL-myc:ptxA*
230 *and Gnai2*$^{del}$*; Gnai3*$^{flox}$; Figure 2E). The phenotypic series moved towards increasingly
231 immature-looking hair bundles, and increasingly mimicked severe defects in *Gpsm2*
232 mutants (Mauriac et al, 2017; Tadenev et al, 2019; Tarchini et al, 2016).
233
234 To quantify and compare hair bundle truncations in OHC, we measured the length of the
235 half-bundle 'wings' on each side of the central vertex. We limited this analysis to mutant
236 strains where hair bundles retained a recognizable vertex, thus excluding *LSL-myc:ptxA*
237 and *FoxG1-Cre; Gnai2*$^{del}$*; Gnai3*$^{flox}$. We then plotted paired left and right values for each
238 OHC and tested length variance for each mutant (Figure 2G; Figure 2 Supp. 1G). In
239 *Gnai1*, *Gnai2* and *Gnai1; Gnai2* mutants, the two wings of each hair bundle had similar
240 lengths, and variance was similar to control littermates. In contrast, variable truncation of
241 one wing in *Gnai3* and *Gnai1; Gnai3* mutants resulted in significantly higher length
242 variance compared to controls (Figure 2G; Figure 2 Supp. 1G). In both *Gnai3* and *Gnai1;*

243 *Gnai3* mutants, 49% of hair bundles had wings of more different lengths than the worst
244 OHC outlier in littermate controls (see Source Data file).
245
246 In conclusion, all GNAI/O proteins are not equally involved in hair bundle morphogenesis,
247 with GNAI3 playing a particularly prominent role. GNAI2 makes a clear contribution since
248 *Gnai3* mutant stereocilia defects dramatically increase in severity when GNAI2 is also
249 absent in *Gnai2; Gnai3* double mutants. These results confirm previous conclusions
250 (Beer-Hammer et al, 2018). In addition, we largely rule out that GNAO is involved in apical
251 HC differentiation. More severe defects in *Gnai1; Gnai3* double mutants compared to
252 *Gnai3* single mutants may indicate that GNAI1 plays a subtle role. However, we cannot
253 rule out differences in genetic background as the underlying cause since $Gnai3^{neo}$ is in
254 mixed (29S1/SvImJ; C57BL/6J) and $Gnai1^{neo}$; $Gnai3^{neo}$ is in pure 129S1/SvImJ
255 background (Supp. Table 1). GNAI1 thus has at best a minimal role in hair bundle
256 development.
257
258 **Only GNAI3 is required for normal auditory brainstem thresholds**
259 To pair morphological defects with auditory function, we next tested Auditory Brainstem
260 Response (ABR) in mutants and control littermates at 3 to 4 weeks of age. Anesthetized
261 animals were presented with pure tone stimuli of decreasing sound pressure intensity (dB
262 SPL) at 8, 16, 32 and 40 kHz and ABRs were recorded with a subcutaneous probe (see
263 Methods). Mirroring their overtly normal apical HC morphology, *Gnai1*, *Gnai2* and *Gnai1;*
264 *Gnai2* mutants showed thresholds comparable to littermate controls at all frequencies
265 (Figure 3A-C). Similarly, constitutive ($Gnao1^{neo}$) or conditional (*Atoh1-Cre;* $Gnao1^{flox}$) loss
266 of GNAO did not alter ABR thresholds (Figure 3 Supp. 1A-B). In contrast, *Gnai3* mutants
267 were profoundly deaf at 32 and 40 kHz and displayed significantly elevated thresholds at
268 8 and 16 kHz compared to littermate controls (Figure 3D). *Gnai1; Gnai3* double mutants
269 shared a similar ABR profile as *Gnai3* single mutants, with apparently higher thresholds
270 at 8 and 16 kHz although these two strains were not compared as littermates (Figure 3D).
271 Littermate controls for *Gnai1; Gnai3* double mutants were homozygote for $Gnai1^{neo}$
272 ($Gnai1^{neo/neo}$; $Gnai3^{neo/+}$) and appeared to have higher thresholds than littermate controls
273 for *Gnai3* mutants ($Gnai3^{neo/+}$) at 32 and 40 but not 8 and 16 kHz, whereas loss of GNAI1

274 did not impact auditory thresholds on its own (Figure 3A). These results match possibly
275 more severe hair bundle defects when GNAI1 is inactivated along with GNAI3 (Figure
276 2C-F), and here again, could reflect either a difference in genetic background or a limited
277 role for GNAI1.
278
279 In summary, we confirm that GNAI3, but not GNAI2, is essential for proper auditory
280 thresholds, as previously proposed (Beer-Hammer et al, 2018). We also clarify that
281 GNAO does not participate. Beer-Hammer and colleagues previously showed that
282 inactivating GNAI2 worsens hearing loss in the *Gnai3* null background, as tested in their
283 *FoxG1-Cre; Gnai2*$^{flox/flox}$*; Gnai3*$^{flox/flox}$ adults (Beer-Hammer et al, 2018). Using a
284 comparable yet distinct model (*FoxG1-Cre; Gnai2*$^{del/del}$*; Gnai3*$^{flox/flox}$), we were largely
285 unable to obtain young adults and thus could not perform ABR. This suggests that our
286 model is more severely affected, and would probably lack ABRs, similar to *FoxG1-Cre;*
287 *Gnai2*$^{flox/flox}$*; Gnai3*$^{flox/flox}$ (Beer-Hammer et al, 2018) and *LSL-myc:ptxA* (Tarchini et al,
288 2016).
289
290 **Distribution of individual GNAI proteins in neonate hair cells**
291 Next, we attempted to define how individual GNAI/O proteins localize in neonate HC.
292 GNAI/O proteins are close paralogs, with mouse and human GNAI1 and GNAI3 most
293 similar in the GNAI group, and GNAO more divergent compared to all GNAI (Figure 1A).
294 Validating and using specific antibodies would thus be challenging. Instead, we used one
295 commercial antibody raised against GNAI3 (scbt"GNAI3") and one antibody raised
296 against GNAI2 (pt"GNAI2") and systematically immunolabeled our mouse model
297 collection to tease apart protein-specific behavior.
298
299 Both antibodies produced the familiar GNAI pattern of enrichment at the bare zone and
300 at row 1 stereocilia tips (Figure 4; arrows and arrowheads, respectively) (Tarchini et al,
301 2013; Tarchini et al, 2016). Both antibodies revealed generally normal GNAI enrichment
302 in *Gnai1* (Figure 4A), *Gnai2* (Figure 4B), and *Gnai1*; *Gnai2* mutants (Figure 4C). This
303 indicates that pt"GNAI2" is not specific for GNAI2 and can also detect GNAI3. In *Gnai3*
304 and *Gnai1; Gnai3* mutants, both antibodies still detected GNAI protein at the bare zone

305 and at stereocilia tips although some HC displayed incomplete enrichment (Figure 4D-
306 E; detailed analysis below, Figure 5). This indicates that scbt"GNAI3" is not specific for
307 GNAI3 and can also detect GNAI2. Finally, neither antibody detected consistent signal
308 over background in *Gnai2; Gnai3* double mutants where GNAI1 is the only GNAI protein
309 remaining (Figure 4F; *FoxG1-Cre; Gnai2*$^{del/del}$*; Gnai3*$^{flox/flox}$). To test experimentally
310 whether these antibodies can detect GNAI1, we first electroporated *Gnai1*, *Gnai2* or
311 *Gnai3* constructs in E13.5 inner ears and cultured the cochlea for 6 days before
312 immunolabeling. Overexpressed *Gnai1* was efficiently detected by pt"GNAI2" but not by
313 scbt"GNAI3" whereas, as expected, overexpressed *Gnai3* was detected by scbt"GNAI3"
314 (Figure 4 Supp. 1A). We next used pt"GNAI2" to immunolabel the gallbladder epithelium
315 where *Gnai1* expression was specifically reported (mousephenotype.org; *LacZ* reporter
316 in *Gnai1*$^{tm1a(EUCOMM)Wtsi}$ strain). Signals were visibly reduced in *Gnai1* mutants compared
317 to littermate controls (Figure 4 Supp. 1B).
318
319 Together, these results indicate that a) GNAI2 and GNAI3 share the same polarized
320 distribution pattern at the bare zone and at stereocilia tips, and b) GNAI1 is absent or
321 hidden by background signals at the HC apical surface since it can be detected by the
322 pt"GNAI2" antibody in other contexts. Loss of GNAO in the *Gnao1*$^{neo}$ or *Atoh1-Cre;*
323 *Gnao1*$^{flox}$ models did not alter signals obtained with scbt"GNAI3" (Figure 4 Supp. 1C-D).
324 Moreover, a GNAO antibody produced unpolarized apical signals that proved unspecific
325 since they were unchanged in *Atoh1-Cre; Gnao1*$^{flox/flox}$ mutants (Figure 4 Supp. 1E). Thus,
326 GNAO likely does not contribute to HC polarization, as also suggested by normal hair
327 bundles and normal ABR thresholds in *Gnao1* mutants.
328
329 **GNAI2 only partially spans the bare zone and stereocilia tips and partially rescues**
330 **hair bundle development in postnatal hair cells lacking GNAI3**
331 We next took a closer look at incomplete GNAI enrichment in *Gnai3* and *Gnai1; Gnai3*
332 mutant HC (Figure 4D-E). In both models, we observed an identical outcome at the P0
333 cochlear base where remaining GNAI was unable to fully and consistently occupy the HC
334 sub-domains when GNAI3 was missing (Figure 5A-B; bare zone, arrows; stereocilia tips,
335 arrowheads). In *Gnai1;* Gnai3 double mutants, the GNAI protein detected is by default

336 GNAI2, and this is likely also true in single *Gnai3* mutants since GNAI1 is not observed in
337 HC (Figure 4F). Because in all cases GPSM2 co-localized with GNAI2 (Figure 5A-B),
338 these results demonstrate that both GNAI2 and GNAI3 can form a complex with GPSM2
339 in HC. Intriguingly, the absence of GPSM2-GNAI2 on one side of the bare zone at P0
340 appeared to coincide with its absence at stereocilia tips on the corresponding side (Figure
341 5A-B). We thus quantified GNAI2 intensity at the bare zone and at stereocilia tips in half-
342 OHC in *Gnai1; Gnai3* mutants. While as expected control OHC showed little variation in
343 GNAI enrichment in either compartment (Figure 5 Supp. 1A), mutant OHC showed highly
344 variable signals that were significantly correlated between the bare zone and tips in the
345 same half-OHC (Figure 5C). Analyzing HC at different stages and tonotopic positions
346 clarified that GNAI2 is progressively unable to compensate for missing GNAI3. At E18.5,
347 the GPSM2-GNAI2 complex could still occupy the totality of the bare zone in *Gnai1; Gnai3*
348 mutants (Figure 5 Supp. 1B), suggesting that GNAI2 fully compensates for the loss of
349 GNAI3 in embryonic HC. At later stages of HC differentiation, partial compensation by
350 GNAI2 observed at P0 (Figure 5A-C) evolved into a lack of compensation by P6 at the
351 cochlear base, where GNAI2 was no longer detected consistently at the tips of stunted
352 stereocilia in mutant IHC (Figure 5D). In contrast, less mature P6 IHC at the cochlear mid
353 position retained partial GNAI2 enrichment correlated between the bare zone and tips
354 (Figure 5E), as seen at P0 (Figure 5A-B).
355
356 The progressive inability of GNAI2 to cover for GNAI3 in individual HC helps explain the
357 unique profile of apical defects in *Gnai3* and *Gnai1; Gnai3* mutants. Loss of GPSM2-
358 GNAI2 in one wing of the OHC hair bundle led to stereocilia degeneration by P8 (Figure
359 5F). One-sided loss of global GNAI function at stereocilia tips is thus likely the origin of
360 truncated hair bundle wings observed in adults *Gnai3* and *Gnai1; Gnai3* mutant OHC
361 (Figure 2G). We divided the P8 OHC apical surface in two halves based on the position
362 of the basal body at the hair bundle vertex, and measured the length of each hair bundle
363 wing as well as the total apical surface area in the same HC half in *Gnai1; Gnai3* mutants
364 (Figure 5F). We found a significant correlation between these two values (Figure 5G;
365 control graph in Figure 5 Supp. 1C), providing further evidence that loss of stereocilia
366 prompts a corresponding loss of flat HC surface area on the same OHC side (Etournay

367 et al, 2010). Finally, we asked whether in time GNAI2 is lost in all stereocilia and along
368 the entire cochlea in *Gnai1; Gnai3* mutants. This proved not to be the case, as GNAI2
369 could still be detected at stereocilia tips in P28 OHC and IHC, although in low and variable
370 amounts compared to GNAI tip signals in littermate controls (Figure 5 Supp. 1D-E).
371
372 In conclusion, GNAI2 could provide a low dose of GNAI protein at stereocilia tips when
373 GNAI3 is missing and preserve elongation and height to some extent. Variable GNAI2
374 amounts thus likely explain why IHC stereocilia have variably reduced heights in absence
375 of GNAI3 (Figure 2B-C; Figure 5D-E), unlike in *Gpsm2* or *LSL-myc:ptxA* mutants where
376 they are more uniformly stunted (Beer-Hammer et al, 2018; Mauriac et al, 2017; Tadenev
377 et al, 2019; Tarchini et al, 2016). Loss of GNAI2 signals that coincides at the bare zone
378 and at stereocilia tips on the same HC side adds to previous evidence suggesting that
379 bare zone enrichment is essential for GPSM2-GNAI trafficking to adjacent row 1
380 stereocilia (Akturk et al, 2022; Jarysta & Tarchini, 2021; Tarchini et al, 2016).
381
382 **Combined loss of GNAI2 and GNAI3 delays and de-polarizes bare zone expansion**
383 **with drastic consequences on stereocilia distribution**
384 Since GNAI2 and GNAI3 show functional redundancy and are the most important GNAI/O
385 proteins for hair bundle differentiation, we next focused on characterizing early HC
386 development in *Gnai2; Gnai3* double mutants (*Foxg1-Cre; Gnai2*$^{del/del}$*; Gnai3*$^{flox/flox}$) and
387 comparing defects to those observed previously with ptx. Unlike at adult stages, *Gnai2;*
388 *Gnai3* double mutants were obtained in close to Mendelian proportions at P0 (see Supp.
389 Table 1). For this goal, we used the new *DIO-ptxA* allele in case the myc tag hindered
390 ptxA activity in the *LSL-myc:ptxA* allele. We first validated the new *Gnai3*$^{flox}$ *and DIO-ptxA*
391 alleles (Figure 2 Supp. 1B, D). As expected, GNAI signals at the bare zone and stereocilia
392 tips were normal in *Gnai3*$^{flox/flox}$ homozygotes but showed a distinctive incomplete pattern
393 along with stunted stereocilia upon Cre recombination (Figure 6 Supp. 1A), as in
394 constitutive mutants (Figure 5A). In fact, the new *DIO-ptxA* model produced identical
395 apical HC defects to the earlier *LSL-myc:ptxA* strain in single HC (Kindt et al, 2021;
396 Tarchini et al, 2016) (Figure 6 Supp. 1B). The fraction of inverted OHC1 in the *DIO-ptxA*
397 model was lower than in the *LSL-myc:ptxA* model when using the postmitotic HC driver

398 *Atoh1-Cre* (Figure 6 Supp. 1C) but identically encompassed 100% of OHC1 with the early
399 *FoxG1-Cre* driver (Figure 6 Supp. 1D). Similar apical HC defects between strains indicate
400 that the N-terminal myc tag and mild *R26* promoter do not limit ptxA activity in *LSL-*
401 *myc:ptxA*. For comparison purposes, we used the *FoxG1-Cre* driver to inactivate
402 GNAI2/GNAI3 and to express ptxA, the same driver used by Beer-Hammer and
403 colleagues (Beer-Hammer et al, 2018).
404
405 Inactivating GNAI2 and GNAI3 abolished the bare zone at E17.5 based on abnormally
406 uniform F-actin signals at the HC surface compared to controls where low F-actin
407 matched GNAI signals (Figure 6A-B; arrows point to the bare zone). In contrast, E17.5
408 *DIO-ptxA* HC had developed a distinct bare zone (Figure 6C, arrows). Measuring its
409 surface area by HC type confirmed that the bare zone was virtually absent in *Gnai2; Gnai3*
410 double mutants but only trended as reduced in ptxA-expressing OHC (Figure 6D). By P0,
411 most *Gnai2; Gnai3* mutant HC at the cochlear base had developed a region lacking
412 microvilli or stereocilia, but its position at the apical surface was highly irregular,
413 complementing extremely dysmorphic hair bundles (Figure 6E-F; arrows point to bare
414 regions). In contrast, P0 *DIO-ptxA* HC displayed largely coherent hair bundles and a
415 polarized bare zone (Figure 6G, arrows). Quantifications revealed a significantly reduced
416 bare area in P0 *Gnai2; Gnai3* mutants compared to littermate controls (Figure 6H),
417 showing that bare zone emergence and expansion is greatly delayed and deregulated in
418 this model (compare P0 in Figure 6H and E17.5 in Figure 6D). In P0 *DIO-ptxA* HC, the
419 bare zone surface area was largely comparable to controls, suggesting that a slight delay
420 in expansion is progressively corrected in time in this model (compare P0 in Figure 6H
421 and E17.5 in Figure 6D). These results best illustrate to date the importance of GPSM2-
422 GNAI for bare zone emergence, expansion and polarized positioning. While both mutant
423 models consistently delay bare zone expansion, differences in timing and severity
424 suggest that ptxA is not as effective as the *Gnai2; Gnai3* double mutant to inhibit GPSM2-
425 GNAI function. This is further underscored by severe stereocilia distribution defects
426 observed in *Gnai2; Gnai3* but not *DIO-ptxA* mutants.
427

428 As reported previously (Kindt et al, 2021; Tarchini et al, 2013; Tarchini et al, 2016), the
429 orientation of OHC1-2 expressing ptxA was inverted compared to controls (Figure 6C, G).
430 Our single *Gnai2; Gnai3* adult mutant sample also appeared to have inverted OHC1
431 based on hair bundle morphology (Figure 2A). However, HC orientation proved
432 challenging to assess in neonate *Gnai2; Gnai3* mutants due to highly dysmorphic hair
433 bundles (Figure 6A-B; E-F). We thus used acetylated tubulin (AcTub) and pericentrin
434 (PCNT) as markers for the kinocilium and the basal body, respectively. This showed that
435 in *Gnai2; Gnai3,* but not in *DIO-ptxA* mutants, the basal body and kinocilium were often
436 in an approximately central position surrounded partially or entirely by stereocilia (Figure
437 6E-F). Rounded perinatal hair bundles are a hallmark of HC where the early off-center
438 migration of the basal body, hence symmetry breaking, is defective.
439
440 To distinguish symmetry-breaking from HC orientation, we next used the position of the
441 basal body at the base of the kinocilium to derive both HC eccentricity and HC orientation.
442 This strategy helped compare the *Gnai2; Gnai3* and *DIO-ptxA* mouse models, and
443 identified two early functions for GNAI before its association with GPSM2 for stereocilia
444 elongation.
445
446 **GNAI proteins drive the off-center migration of the basal body**
447 We used the position of the basal body to measure HC eccentricity as a metric for
448 cytoskeleton asymmetry. Eccentricity was calculated as a ratio reporting how far away
449 from the cell center the basal body was positioned (see schematic in Figure 7). A perfectly
450 symmetrical HC with a central basal body would thus have an eccentricity close to 0
451 whereas a ratio close to 1 would indicate that the off-center basal body is juxtaposed to
452 the apical junction. Because HC maturation progresses in time and along the tonotopic
453 axis (cochlear apex to base gradient of increasing maturity), we measured eccentricity at
454 E17.5 (base and mid cochlear position) and at P0 (base, mid and apex) to understand
455 how eccentricity progressed at the HC population level.
456
457 Control HC at E17.5 had already broken symmetry at the mid position, with eccentricity
458 averaging ~0.5 and increasing at the more mature base position (Figure 7A). At E17.5

459 mid and base positions, *Gnai2; Gnai3* mutant HC showed a significantly reduced
460 eccentricity, suggestive of a delay in the off-center migration of the basal body. We
461 arbitrarily defined 0.25 as a threshold below which HC were considered near-symmetrical.
462 Symmetrical HC were not observed in controls but represented up to ~29% of IHC and
463 ~34% of OHC in *Gnai2; Gnai3* mutants at E17.5 (detailed in Figure 7A by stage, position
464 and HC type; red highlights). By P0, the proportion of symmetrical cells in mutants had
465 decreased at all positions for OHC (3.3-15.2%), but remained high or increased for IHC
466 (21.5-42.4%; Figure 7A).
467
468 The situation was radically different in the *DIO-ptxA* model. First, no symmetrical HC was
469 observed at any stage or position in mutants (Figure 7B). In the *DIO-ptxA* model, the
470 distribution of eccentricity values in IHC was generally similar to controls. By contrast,
471 OHC eccentricity trended as higher in *DIO-ptxA* compared to littermate controls, with the
472 difference becoming less significant with OHC differentiation (Figure 7B). Defective bare
473 zone expansion (Figure 6D, H) can help explain the distinct eccentricity defects in the
474 *DIO-ptxA* (transiently higher eccentricity) and *Gnai2; Gnai3* (lower eccentricity) mouse
475 models. The position of the basal body is the sum of two opposite movements (Figure
476 1B): a) the early off-center migration that brings the basal body in the vicinity of the lateral
477 junction, and b) the subsequent relocalization towards the cell center upon bare zone
478 expansion that brings the basal body in contact with the forming hair bundle (Tarchini et
479 al, 2013). In *DIO-ptxA*, transiently increased eccentricity in OHC is likely the outcome of
480 a normal off-center basal body migration combined with delayed bare zone expansion
481 (Figure 6D, H). In *Gnai2; Gnai3* mutants by contrast, decreased eccentricity in OHC
482 (Figure 7A) stems from defective off-center migration of the basal body combined with an
483 initially absent (E17.5), and then reduced (P0), bare region (Figure 6D, H). When an
484 unpolarized bare region eventually emerges in *Gnai2; Gnai3* mutants (Figure 6H), it
485 impacts basal body position without directionality, leading to highly variable eccentricity
486 values compared to controls (Figure 7A), and thus variably dysmorphic hair bundles. The
487 apparent increase in symmetrical IHC over time in *Gnai2; Gnai3* mutants (Figure 7A) may
488 result from the delayed expansion of the bare region, which will relocalize the basal body
489 centrally in a proportion of IHC.

490

491 In conclusion, symmetry-breaking (Figure 7), bare zone emergence and expansion and
492 stereocilia distribution (Figure 6) are all severely impaired in *Gnai2; Gnai3* mutants. In
493 ptxA mutants in contrast, symmetry-breaking occurs normally, bare zone expansion is
494 only delayed and stereocilia distribution is less affected. It follows that ptxA does not
495 achieve a loss of GNAI2/GNAI3 function as extensive as in *FoxG1-Cre; Gnai2; Gnai3*
496 mutants. This is probably because ptxA only downregulates and does not inactivate
497 GNAI/O proteins, and because ptxA substrates also include GNAI1 and GNAO that could
498 be active in other contexts than polarization in HCs.

499

500 **GNAI proteins orient hair cells laterally**

501 GNAI proteins were proposed to signal downstream of the GPR156 receptor to regulate
502 HC orientation in auditory and vestibular organs (Jiang et al, 2017; Kindt et al, 2021). In
503 HC expressing the transcription factor EMX2, GPR156-GNAI reverses the orientation of
504 the off-center basal body migration, and thus HC orientation, compared to *Emx2*-negative
505 HC (Tona & Wu, 2020). To date, however, the HC misorientation profile observed in *Emx2*
506 or *Gpr156* mutants was only recapitulated using ptxA (Figure 1C) (Kindt et al, 2021). If
507 ptxA-based orientation defects are physiologically relevant to GNAI function, they might
508 be observed in *Gnai2; Gnai3* mutants as well. As mentioned above, a caveat to test this
509 assumption is that highly dysmorphic hair bundles in *Gnai2; Gnai3* mutants obscure HC
510 orientation.

511

512 To circumvent this limitation, we first excluded near-symmetrical HC in the *Gnai2; Gnai3*
513 mutant datasets since an asymmetric cytoskeleton is pre-requisite for HC to exhibit a
514 defined orientation (excluded: eccentricity<0.4 at E17.5 and <0.25 at P0). Next, we used
515 the position of the off-center basal body to infer the orientation of the remaining
516 asymmetric HC, ignoring the shape of the hair bundle. We measured the angle formed
517 by a vector running from the HC center to the basal body relative to the cochlear
518 longitudinal axis ($\alpha$, see schematic in Figure 8). Angles were plotted in circular histograms
519 where 0° points to the cochlear base and 90° to the lateral edge. At E17.5 at the cochlear
520 mid position, *DIO-ptxA* showed the graded pattern of OHC misorientation observed as

521 early as these cells break planar symmetry (Kindt et al, 2021), with inverted OHC1 and
522 OHC2 and imprecisely oriented IHC and OHC3 (Figure 8A). *DIO-ptxA* OHC1-2
523 maintained this misorientation profile at the E17.5 base and at P0 (Figure 8B-D) as well
524 as in adults (Figure 2A).
525
526 At the E17.5 cochlear mid, many but not all OHC1 were strikingly inverted as well in
527 *Gnai2; Gnai3* mutants (Figure 8A). The majority of more mature OHC1 at the E17.5
528 cochlear base were inverted (Figure 8B), as were P0 OHC1 at all positions (Figure 8C-
529 D; Figure 8 Supp. 1A). Loss of GNAI2 and GNAI3 can thus recapitulate inverted OHC1-
530 2 observed in the *DIO-ptxA* model with what appears to be a delay. In contrast however,
531 OHC2 were generally oriented laterally (90°) at E17.5 and at the P0 apex and mid in
532 *Gnai2; Gnai3* mutants (Figure 8A-C; Figure 8 Supp. 1A). OHC2 only adopted inverted
533 orientation characteristic of the *DIO-ptxA* model at the P0 base where HC are more
534 mature (Figure 8D). As OHC2 mature later than OHC1 (Anniko, 1983), this again
535 suggests a delay where GPR156-GNAI signaling can initially reverse OHC1-2 normally,
536 but where a lateral orientation cannot be maintained and OHC1-2 ultimately become
537 inverted as in the *DIO-ptxA* model.
538
539 *FoxG1-Cre* is expressed at the otocyst stage in cochlear progenitors (Hebert &
540 McConnell, 2000) and globally downregulates GNAI/O proteins early on in the *DIO-ptxA*
541 model. However, *FoxG1-Cre*-mediated deletion at the *Gnai3* locus in *Foxg1-Cre*;
542 *Gnai2*$^{del/del}$; *Gnai*$^{flox/flox}$ mutants might preserve some functional GNAI3 proteins for a
543 longer time and explain the apparent delay in OHC1-2 misorientation. To test this idea,
544 we delayed GNAI downregulation by ptxA and asked whether this would result in a milder,
545 delayed OHC1-2 misorientation phenotype as seen in *Gnai2; Gnai3* mutants. For that
546 goal, we used the *Atoh1-Cre* driver which is only active in postmitotic HC (Matei et al,
547 2005). Strikingly, while P0 OHC1 were inverted in *Atoh1-Cre; DIO-ptxA* as in *FoxG1-Cre;*
548 *DIO-ptxA*, OHC2 generally pointed laterally (90°) in *Atoh1-Cre; DIO-ptxA* as in *Gnai2;*
549 *Gnai3* mutants at the E17.5 base and the P0 apex (Figure 8 Supp. 1B). However, a large
550 proportion of OHC2 were inverted at the P0 base, supporting the hypothesis of a delayed
551 inversion following delayed GNAI loss-of-function.

552

553 Together, these results first show that the *ptxA* misorientation pattern is present in *Gnai2;*
554 *Gnai3* double mutants. Differences in severity between models can be explained by
555 different timing of GNAI inactivation. Of note, the only surviving *Gnai2; Gnai3* double
556 mutant we obtained suggests that OHC1-2 inversion is maintained in adults (Figure 2A),
557 as in *ptxA* and *Gpr156* mutants (Figure 2A) (Kindt et al, 2021). Endogenous GNAI proteins
558 are thus integral for OHC1-2 to reverse and adopt a proper lateral orientation during
559 development, and at least transiently to maintain this lateral orientation. Second, these
560 results also suggest that the GNAI activities required for symmetry-breaking, lateral HC
561 orientation and for hair bundle morphogenesis are qualitatively different (Figure 9). *Gnai2;*
562 *Gnai3* mutants are more severely affected considering symmetry-breaking and hair
563 bundle morphogenesis, whereas *DIO-ptxA* mutants appear more severely affected
564 considering OHC1-2 orientation. Of note however, IHC and OHC3 were severely
565 misoriented in *Gnai2; Gnai3* mutants at all stages and positions analyzed, but much less
566 affected in *DIO-ptxA* mutants (Figure 8; Figure 8 Supp. 1A). We discuss below how
567 different GNAI protein identity, dose, timing and upstream regulators may underlie
568 different roles (Figure 9) and explain differences in phenotype across mutant models.

## DISCUSSION

By examining a large collection of single and combined mutations in *Gnai/o* genes (*Gnai1*, *Gnai2*, *Gnai3*, *Gnao1*), we assign here three distinct roles for GNAI proteins during the apical polarization of a developing HC (Figure 9): a) to drive the centrifugal migration of the basal body when a prospective HC breaks planar symmetry and b) to orient this migration along the PCP axis in a binary manner, and c) to position and elongate stereocilia during hair bundle morphogenesis. Key results in the study include demonstrating that endogenous GNAI proteins indeed serve early functions (a) and (b), since to date only hair bundle defects (c) were reported in knock-out mouse models where *Gnai* genes were targeted (Beer-Hammer et al, 2018; Mauriac et al, 2017). Previous studies suggested that GNAI proteins partner with different regulators to fulfill different roles, organizing and elongating stereocilia by binding the scaffold GPSM2 (c), and reversing HC orientation in *Emx2*-expressing HC downstream of the receptor GPR156 (b).

### Different GNAI/O identity, dosage and timing underlie different roles

Interestingly, besides involving different regulators, each role also appears to involve different dosage and specific identity of the underlying GNAI protein(s) at different times during HC development (Figure 9). For postnatal hair bundle morphogenesis (c), GNAI proteins are sequestered in the GDP-bound state by GPSM2, forming a complex highly enriched at the bare zone and at row 1 stereocilia tips that can be reliably immunodetected (Akturk et al, 2022; Kindt et al, 2021). In these two sub-cellular compartments, the identity of the GNAI proteins at work matters, with GNAI3 playing a required and prominent role while GNAI2 is important yet not required. Although one of our GNAI antibodies can detect GNAI1, we did not observe GNAI1 signals in HC (Figure 4), and *Gnai1* mutants did not exhibit significant hair bundle defects or ABR threshold shifts (Figure 2; Figure 3A). On the other hand, we observed a trend towards more severe stereocilia defects and more elevated ABR thresholds in *Gnai1; Gnai3* compared to single *Gnai3* mutants (Figure 2C-E; Figure 3D). Together, these results suggest that GNAI1 plays a minor, or no role in hair bundle development, with differences in the genetic

background between strains possibly explaining the latter results. Similarly, we did not observe HC or auditory defects in absence of GNAO.

In stark contrast with its inability to rescue hair bundle morphogenesis (c), GNAI2 can fully rescue the off-center migration of the basal body (a) and its direction which defines HC orientation (b) when both GNAI1 and GNAI3 are constitutively absent. These two early roles are qualitatively different because they do not strictly reflect a difference in timing (a and b occur at the same time) or GNAI/O dose. Symmetry-breaking (a) is affected in *Gnai2; Gnai3* double mutants but is intact in the *ptxA* model despite early (*FoxG1-Cre*) and high (caggs promoter) expression of untagged pertussis toxin. On the contrary, orientation of OHC1-2 (but not IHC and OHC3) is most severely affected in the *DIO-ptxA* model, with *Gnai2; Gnai3* mutants showing delayed defects. PtxA downregulates but does not abolish GNAI/O proteins, and we thus conclude that ptxA cannot achieve a loss of GNAI2 and GNAI3 function as extensive as in double targeted mutants. Among GNAI/O proteins, GNAI2 and GNAI3 may be more specifically required for HC to break symmetry, but other GNAI/O proteins and/or other factors may participate as well since a majority of HC eventually break symmetry even in *Gnai2; Gnai3* mutants. On the other hand, GPR156 is known to signal via heterotrimeric GNAI proteins (Watkins & Orlandi, 2021), and we speculate that any GNAI/O protein may equally relay signals to regulate HC orientation. PtxA would thus be a particularly effective way to disrupt the orientation role (b), with GNAI1 and/or GNAO partially rescuing orientation in *Gnai2; Gnai3* mutants. Our results also suggest that GNAI/O proteins are not only required for OHC1-2 to adopt a normal lateral instead of medial orientation upon symmetry-breaking (normal GPR156-driven reversal; Figure 9), but also to maintain this lateral orientation, at least transiently. Delayed GNAI/O inactivation indeed appears to result in initially normal OHC1-2 lateral orientation followed by a switch to medial orientation in a proportion of cells (abnormal inversion; Figure 8; Figure 8 Supp. 1B).

Regarding dosage, we propose that embryonic activities (a, b) run on low GNAI/O amounts compared to hair bundle functions (c). Of note, GNAI/O proteins are not immunodetected along with GPR156 in HC (b) but are easily detected with GPSM2 at the

631 bare zone and stereocilia tips (Akturk et al, 2022; Kindt et al, 2021). This may be because
632 GNAI/O proteins in heterotrimeric G protein complexes cycle dynamically between a GDP
633 and GTP-bound state at low dose and escape immunodetection. In this context, it should
634 be noted that a GNAI/O regulator for symmetry-breaking and its mode of action remain
635 unknown (Figure 9, role a).
636
637 A time- and dosage- dependence for early GNAI roles can explain why our conditional
638 *Gnai2; Gnai3* double mutant model is more severely affected than a comparable
639 conditional *Gnai2; Gnai3* model where only hair bundle defects (c) were reported (Beer-
640 Hammer et al, 2018). While Beer-Hammer and colleagues used *FoxG1-Cre* as a driver
641 as we did, combined GNAI2 and GNAI3 inactivation necessitated Cre recombination at
642 four floxed loci (*Gnai2*$^{flox/flox}$*; Gnai3*$^{flox/flox}$). In contrast, our model necessitates
643 recombination at two loci only (*Gnai2*$^{del/del}$*; Gnai3*$^{flox/flox}$). We thus conclude that our model
644 achieves an earlier and further loss of GNAI2/GNAI3 activity. This hypothesis is supported
645 by extensive postnatal lethality in our model, whereas Beer-Hammer and colleagues
646 could analyze *Gnai2; Gnai3* double mutants as adults. Our work thus usefully reconciles
647 previous reports about GNAI functions in HC, notably showing that inactivating
648 endogenous GNAI proteins does produce early defects (a,b) so far only observed with
649 ptx. We thus validate all HC defects observed with ptx as physiologically relevant and
650 specific to GNAI/O function.
651
652 **Hair cell break of symmetry**
653 Although cochlear HC expressing ptxA undergo normal symmetry-breaking in vivo (this
654 work and (Kindt et al, 2021; Tadenev et al, 2019; Tarchini et al, 2013; Tarchini et al,
655 2016)), a fraction of utricular and saccular HC expressing myc:ptxA showed an
656 abnormally central basal body (Kindt et al, 2021). This suggests that a higher dose of
657 GNAI/O is required for the off-center migration of the basal body in vestibular compared
658 to cochlear HC, making vestibular HC more susceptible to ptxA. “Ciliary” proteins are
659 required for ciliogenesis, including kinocilium formation and maintenance, and also play
660 non-ciliary functions (May-Simera et al, 2015; Sipe & Lu, 2011). Inactivation of
661 intraflagellar transport protein IFT88 was reported to result in a central basal body and

662 circular hair bundles in ~10% of OHC (Jones et al, 2008), but the underlying mechanism
663 was not elucidated. A low proportion of symmetrical HC was also reported in absence of
664 the CD2 isoform of the protocadherin PCDH15 that forms inter-stereocilia and kinocilium-
665 stereocilia fibrous links during embryogenesis (Webb et al, 2011). It remains unclear
666 whether GNAI/O activity participates in *Ift88* or *Pcdh15* mutant defects, or whether GNAI
667 could be active at the basal body or the kinocilium.
668
669 **Hair cell orientation**
670 The planar cell polarity (PCP) axis is defined by opposite asymmetric enrichment of the
671 core PCP transmembrane proteins VANGL2 and FZD3/6 and their specific cytosolic
672 partners at the apical junction of HC and support cells (Deans, 2013; Montcouquiol &
673 Kelley, 2019; Tarchini & Lu, 2019). Previous work showed that regional *Emx2* expression
674 reverses how the HC basal body migrates relative to uniform and early-set core PCP
675 landmarks, notably establishing the line of polarity reversal in the utricle and saccule.
676 EMX2 activates the GPR156 receptor by triggering its polarized enrichment at the apical
677 HC junction, where downstream GNAI/O signaling appears to reverse how core PCP
678 cues are interpreted and to repel the basal body (Figure 9, role b) (Kindt et al, 2021).
679 EMX2 achieves this goal by preventing expression of the kinase STK32A that suppresses
680 apical enrichment and polarization of the GPR156 protein (Jia et al, 2023). It is important
681 to note that HC lacking GPR156 have a normal apical cytoskeleton, including a normally
682 formed hair bundle, and only show orientation defects (Kindt et al, 2021). This indicates
683 that the centrifugal migration of the basal body and the direction of this migration that
684 defines early HC orientation are two distinct molecular mechanisms although both involve
685 GNAI/O proteins (Figure 9; a *versus* b). Similarly, HC lacking GPSM2 are not inverted in
686 orientation as in *Emx2*, *Gpr156*, *Gnai2; Gnai3* or *ptxA* mutants (Bhonker et al, 2016; Ezan
687 et al, 2013; Tarchini et al, 2013). This indicates that bare zone enrichment of the GPSM2-
688 GNAI complex is a mechanism to shape and polarize the growth of the hair bundle, but
689 not to migrate off-center or orient the basal body. GPSM2-GNAI is polarized on the side
690 of the off-center basal body but occupies the HC apical membrane and not the apical
691 junction where core PCP proteins regulate HC orientation (Siletti et al, 2017; Tarchini et
692 al, 2013).

While both GPR156 (Greene et al, 2023; Ramzan et al, 2023) and GPSM2 (Doherty et al, 2012; Walsh et al, 2010) have been identified as human deafness genes, there is currently no evidence implicating a GNAI/O protein. This is most likely because all GNAI/O proteins, including GNAI3 which is more specifically required in HC for hair bundle morphogenesis (Figure 9), play ubiquitous and critical signaling roles in the context of heterotrimeric protein signaling across many cell types.

701 **METHODS**

702

703 **Mouse strains and husbandry**

704 All mouse strains used in this work and strain-related information is summarized in
705 Supplementary Table 1. All primers used for genotyping are indicated in Supplementary
706 Table 2 by strain.

707 Strains from The Jackson Laboratory repository: *Gnai1*$^{neo}$*; Gnai3*$^{neo}$ (*Gnai1*$^{tm1Lbi}$*;*
708 *Gna3*$^{tm1Lbi}$*;* MGI: 5560183) (Jiang et al, 2002) carries a neo cassette in *Gnai1* exon 3 and
709 a neo cassette replacing part of intron 5 and exon 6 in *Gnai3* in the 129S1/SvImJ
710 background. The single *Gnai1*$^{neo}$ and single *Gnai3*$^{neo}$ alleles were segregated from
711 *Gnai1*$^{neo}$*; Gnai3*$^{neo}$ by breeding with C57BL/6J mice and are consequently on a mixed
712 129S1/SvImJ: C57BL/6J background. *Gnao1*$^{neo}$ (*Gnao1*$^{tm1Lbi}$; MGI: 2152685) carries a
713 neo cassette in *Gnao1* exon 6 in the 129S1/SvImJ background (Jiang et al, 2002). The
714 two *Cre* strains used in this work are *Atoh1-Cre* (*Tg(Atoh1-cre)1Bfri;* MGI: 3775845)
715 expressing Cre in HC from E14.5 (Matei et al, 2005) and *FoxG1-Cre* (*Foxg1*$^{tm1(cre)Skm}$;
716 MGI: 1932522) expressing Cre in the prospective otic vesicle from E8.5 (Hebert &
717 McConnell, 2000).

718

719 Consortium strain: *Gnao1*$^{flox}$ (*Gnao1*$^{tm1c(EUCOMM)Hmgu}$) was derived from the EUCOMM
720 strain *Gnao1*$^{tm1a(EUCOMM)Hmgu}$ (MGI: 4456727; "KO first, conditional ready"). The *Gnao1*$^{flox}$
721 conditional allele was produced via FLP-mediated recombination (FLP strain MGI:
722 4830363) to remove the FRT-flanked *LacZ-neo* cassette, leaving exon 3 floxed. *Gnao1*$^{flox}$
723 is on C57BL/6N background.

724

725 Constitutive *Gnai2*$^{del}$ inactivation (see Figure 2 Supp. 1A). *Gnai2*$^{del}$ (*Gnai2*$^{em1Btar;}$ MGI:
726 6466534) was generated using delivery of CRISPR-Cas9 reagents in mouse zygotes via
727 electroporation. The following guide RNAs (gRNAs) were used to delete exon 2, exon 3
728 and part of exon 4 in the C57BL/6J background. Upstream gRNA:
729 CTGCCCTCTGTTCCAGGTGC, downstream gRNA: ATGCTTCCTGAAGACCTGTC.
730 The resulting 681 bp deletion encompassed
731 TGCTGGAGAGTCAGGGAAGA...CCTGAAGACCTGTCCGGTGT. The electroporation

732 mixture consisted of the gRNAs with AltR- *Streptococcus pyogenes* Cas9 (SpCas9) V3
733 (Integrated DNA Technologies #1081059) in embryo-tested TE buffer (pH 7.5).
734 Electroporation of zygotes was performed as described in (Qin et al, 2015). In order to
735 segregate away potential non-specific mutations, founders were bred for two generations
736 with C57BL/6J animals to generate a N2 heterozygote stock. Because *Gnai2*$^{del}$
737 homozygotes showed low viability, this strain was used in a mixed C57BL/6J:FVB/J
738 background that improved the proportion of homozygotes (see Supp. Table 1).
739
740 Conditional *Gnai3*$^{flox}$ inactivation (see Figure 2 Supp. 1B). A plasmid-based donor vector
741 was cloned to flank *Gnai3* exon 2 and 3 with *loxP* sites using the same CRISPR/Cas9
742 system as described above for *Gnai2*$^{del.}$ A fragment carrying a *loxP*, a genomic region
743 including exon 2-3, the restriction site ClaI, a second *loxP* and the restriction site XhoI
744 was synthetized (Genscript) and cloned between 5' and 3' homology arms amplified by
745 PCR using Gibson assembly. The following gRNAs were used and define the extremities
746 of the floxed region: upstream, AGCTCACCAAAATTCCCATT,
747 TAGGGGATATAGATCCAAAT, downstream, TTCCAGGACTCTGCATGCGT,
748 TACCGACGCATGCAGAGTCC. The gene editing reagents (gRNAs, donor vector,
749 SpCas9) were microinjected in zygotes as described in (Qin et al, 2015). To confirm
750 insertion at the *Gnai3* locus, we performed long-range PCRs with a genomic primer
751 located outside the homology arm on each side: *5' long-range:* F(external)_
752 TACTGAGATGAGAGACTGAGGG and R (internal)_TGGCTGACATCCTTTGATGGAC.
753 The 3070 bp product was digested with XhoI, producing 2,551 + 519 bp fragments upon
754 donor insertion (flox allele). 3' long-range: F
755 (internal)_TGAAAGGTAAAGGCAACGTGAG and R
756 (external)_TGTGAGACAGGGTCTCTCTTTG. The 2,966 bp product was digested with
757 XhoI, producing 2,000 + 966 bp fragments upon donor insertion (flox allele). In order to
758 segregate away potential non-specific mutations, founders were bred for two generations
759 with C57BL/6J animals to generate a N2 heterozygote stock.
760
761 Pertussis toxin catalytic subunit (ptxA)-expressing strains (see Figure 2 Supp. 1C-D). The
762 *LSL-myc:ptxA* strain at the *ROSA26* (*R26*) locus was described previously

763 (*Gt(ROSA)26Sor*$^{em1(ptxA)Btar}$; MGI: 6163665) (Tarchini et al, 2016). The new *CAG-DIO-*
764 *ptxA* strain line (see Figure 2 Supp. 1D) was generated at the *R26* locus using the Bxb1
765 attP(GT) integrase technology and *C57BL/6J-Gt(ROSA)26Sor*$^{<em2Mvw>/Mvw}$ (MGI:
766 6757188) as the host strain (Low et al, 2022). The donor vector consisted in a CAG
767 promoter followed by the flipped ptxA coding sequence flanked by double inverted lox
768 sites (loxP and lox2272; Figure 2 Supp. 1D) and a bGHpA sequence. In order to exclude
769 the prokaryotic vector backbone, the donor vector was prepared as a minicircle using the
770 MC-Easy Minicircle Production kit (SystemBio, MN920A-1). Briefly, the donor plasmid
771 insert was cloned into a Minicircle Cloning Vector using PhiC31 integrase before
772 transformation into the ZYCY10P3S2T *E. coli* minicircle producer strain, which after
773 induction with arabinose, results in the generation of the donor minicircle. To eliminate
774 parental plasmid contamination, a restriction digest was performed, followed by MC-safe
775 DNase treatment. The minicircle DNA was then purified by phenol-chloroform extraction
776 and reconstituted in microinjection buffer (10 mM Tris; 0.1 mM EDTA pH7.5). The *CAG-*
777 *DIO-ptxA* strain was generated by pronuclear microinjection of the Bxb1 Integration
778 reagents directly into zygotes of the host strain. These reagents included the Bxb1 mRNA
779 (Trilink) at 100ng/µl, RNasin (Promega) at 0.2U/µl and the donor minicircle DNA at
780 10ng/µl combined in microinjection buffer. To confirm successful integration of the
781 3,212bp transgene, as well as identify random transgenics, the initial screening was
782 performed using a four-PCR strategy. The In/Out Left and Right (IOL, IOR) PCRs, which
783 bridge the recombined attachment sites, each contain one primer specific to the *R26*
784 locus and a second primer designed against the inserted sequence. The Transgene (TG)
785 PCR amplifies a non-genomic sequence in the insert, and the Off-Target Integration (OTI)
786 PCR was designed to detect non-recombined minicircle integration, presumably outside
787 of the *R26* locus.
788 IOL PCR (F1/R1), F1: GTCGCTCTGAGTTGTTATCAGT, R1:
789 GCCAAGTAGGAAAGTCCCATAA (720 bp, WT=no band). IOR PCR (F2/R2), F2:
790 GGTGATGCCGTTGTGATAGA, R2: TGTGGGAAGTCTTGTCCCTCCAAT (1,013 bp,
791 WT=no band). TG PCR (F2/R3) F2: 5'-GGTGATGCCGTTGTGATAGA, R3:
792 CCACTTCATCGGCTACATCTAC (214 bp, WT=no band). OTI PCR (F3/R1) F3:
793 GGGAGGATTGGGAAGACAATAG, R1: GCCAAGTAGGAAAGTCCCATAA (578 bp,

794 WT=no band). 33 mice were born following 6 transfers totaling 117 injected embryos
795 (28% survival), and 1/33 (3%) was identified as a founder and crossed to C57BL6/J to
796 generate N1 offspring. The In/Out PCR confirmed that a copy of the transgene was
797 inserted at the *R26* locus, but the OTI strategy also gave a product, even after breeding
798 for multiple generations. As breeding would have segregated a separate, random
799 integration of the transgene, we performed Nanopore-based Cas9-targeted sequencing
800 at the *R26* locus (Gilpatrick et al, 2020; Low et al, 2022). This revealed that, as seen in
801 some cases previously (Low et al, 2022), tandem insertion had occurred in this founder
802 Specifically, 3 consecutive copies of the *CAG-DIO-ptxA* transgene were inserted at the
803 *R26* locus in this strain. This did not impact specific Cre-based expression of ptxA
804 because phenotypes observed in this new strain were comparable to the previous *LSL-*
805 *myc:ptxA* strain (Figure 6 Supp.1 B-D).
806
807 Experimental animals in the study ranged in age between E17.5 and P29 as indicated in
808 each figure. Male and females were systematically included but sex was not tracked
809 except for Auditory Brainstem Recordings because there is no evidence that sex
810 influences HC orientation or hair bundle morphogenesis. Animals were maintained under
811 standard housing conditions (14h light / 10h dark cycle, ambient temperature and normal
812 humidity). All animal work was reviewed for compliance and approved by the Animal Care
813 and Use Committee of The Jackson Laboratory (Animal Use Summary AUS #14012).
814
815 **Scanning Electron Microscopy (SEM)**
816 Temporal bones were isolated, punctured at the cochlear apex, and fixed by immersion
817 for at least one overnight at 4°C in 2.5% glutaraldehyde (Electron Microscopy Sciences;
818 16200) and 4% paraformaldehyde (Electron Microscopy Sciences; 15710) in 1mM $MgCl_2$,
819 0.1M Sodium Cacodylate, 20mM $CaCl_2$. Samples were rinsed and decalcified overnight
820 in 4% EDTA. The auditory epithelium was then dissected into 3 pieces (cochlear base,
821 mid, and apex) before progressive dehydration in an ethanol series (30-50-70-80-90-
822 100%, at least 20 minutes per step) and chemical drying with hexamethyldisilazane
823 (HMDS; Electron Microscopy Sciences 50-243-18). Dry samples were mounted on

824 aluminum stubs using double-sided carbon tape and sputter-coated with gold-palladium
825 before imaging on a Hitachi 3000N VP electronic microscope at 20kV.
826
827 **Immunofluorescence and antibodies**
828 For embryonic and postnatal stages, temporal bones were immediately dissected to
829 expose the sensory epithelium and fixed in paraformaldehyde (PFA 4%; Electron
830 Microscopy Sciences; 15710) for 1h at 4°C. After fixation, the tectorial membrane was
831 removed, and samples were permeabilized and blocked in PBS with 0.5% Triton-X100
832 and bovine serum albumin (1%) for at least at 1 hour at room temperature. For adult
833 stages, temporal bones were isolated and punctured at the cochlear apex to facilitate
834 access of the fixative. Samples were then immersion-fixed in PFA 4% for 1 hour at 4°C,
835 rinsed in PBS, and incubated overnight in 4% EDTA for decalcification. Cochleae were
836 next dissected in 3 pieces (cochlear base, mid, and apex), before permeabilization and
837 blocking as described above. Primary and secondary antibodies were incubated
838 overnight at 4°C in PBS with 0.025% sodium azide. Fluorescent dye-conjugated
839 phalloidin was added to secondary antibodies. Samples were washed 3 times in PBS +
840 0.05% Triton-X100 after each antibody incubation and post-fixed in PFA 4% for at least
841 1 hour at room temperature. Samples were then mounted flat on microscopy slides
842 (Denville M102) using Mowiol as mounting medium (Calbiochem/MilliporeSigma
843 4759041), either directly under a 18x18mm #1.5 coverglass (VWR 48366-045) (postnatal
844 cochleae) or using one layer of office tape as a spacer (adult cochleae). Mowiol (10%
845 w/v) was prepared in 25%(w/v) glycerol and 0.1M Tris-Cl pH8.5. Primary antibodies used
846 were:
847
848 Rabbit anti-GNAI2, pt"GNAI2" (Proteintech, 11136-1-AP); the antigen is the full human
849 GNAI2 protein
850 Rabbit anti-GNAI3, scbt"GNAI3" (Santa Cruz Biotechnology, sc-262); the antigen is
851 undisclosed but corresponds to a C-terminal region of the rat GNAI3 protein
852 Rabbit anti-GNAO (Proteintech, 12635-1-AP)
853 Mouse anti-acetylated alpha tubulin (Santa Cruz Biotechnology scbt-23950)
854 Rabbit anti-GPSM2 (Sigma, A41537)

855 Goat anti-GPSM2 (Thermofisher, PA5-18646)
856 Rabbit anti-Pericentrin/PCNT (Biolegend/Covance, PRB-432C)
857 Rat anti-ZO1 (Developmental Studies Hybridoma Bank, R26.4C)
858
859 Secondary antibodies from ThermoFisher Scientific were raised in donkey and
860 conjugated to Alexa Fluor (AF) 488, 555, or 647 (donkey anti-rabbit AF555 (A-31572),
861 AF647 (A-31573), donkey anti-mouse AF647 (A-31571), donkey anti-rat AF488 (A-
862 21208), donkey anti-goat AF555 (A-21432), AF647 (A-21447)). Fluorescent conjugated
863 phalloidins used to reveal F-actin were from ThermoFisher Scientific (AF488 (A12379);
864 AF555 (A34005)) and Sigma-Aldrich (FITC (P5282)).
865
866 **Inner ear electroporation and cochlear culture**
867 Inner ears from wild-type animals (mixed C57BL/6J-FVB/NJ background) were harvested
868 at E13.5 in HBSS/5mM Hepes. Caggs plasmid vectors (CMV early enhancer, beta-actin
869 promoter) driving either mouse *Gnai1*, *Gnai2* or *Gnai3* cDNA expression were mixed with
870 Fast Green FCF (0.05%; Sigma, F7252) and injected at 2.5mg/ml in the cochlear duct
871 using a Wiretroll capillary and plunger (Drummond, 53507-426). Injected inner ears were
872 next electroporated (BTX ECM830; 27V, 27 ms, 6 square pulses at 950 ms intervals), the
873 condensed mesenchyme was dissected away and the soft cochlear labyrinth was
874 embedded in 50% Matrigel (Corning, CB40234). Cochlear explants were cultured for 6
875 days in DMEM with 10% fetal bovine serum and 10 µg/ml ciprofloxacin (Sigma, 17850).
876 Explants were then fixed in 4% PFA for 15 min at room temperature before being
877 processed for immunolabeling.
878
879 **Sample cohorts, image acquisition and analysis**
880 All quantifications include at least three animals per genotype. All graphs or their legends
881 indicate the animal cohort size (N) as well as the number of HC or stereocilia (n) analyzed.
882 Further details can be found in the Supplementary Source Data file where tabs are
883 referencing figure panels in order. When an experimental outcome was not quantified, at
884 least 3 mutant and 3 control littermates encompassing two or more litters were analyzed,
885 and figure panels illustrate a representative outcome observed in all samples of the same

genotype. A single exception is adult *Foxg1-Cre; Gnai2*$^{del/del}$*; Gnai3*$^{flox/flox}$ data in Fig. 2A-F where a single mutant animal was analyzed since we failed to obtain others at 3 weeks of age in spite of extensive breeding (see Supp. Table 1).

Confocal images were captured with a LSM800 line scanning confocal microscope, a 63x NA1.4 oil objective, the Airyscan detector in confocal mode (except in Figure 5 Supp.1 D, E where the Airyscan detector was used in Airyscan mode) and the Zen 2.3 or Zen 2.6 software (Carl Zeiss AG). Raw Airyscan images in Figure 5 Supp.1 D, E were processed in Zen 2.6 selecting for automatic strength. Unless stated otherwise in the legends, images show a single optical z plane. To quantify HC eccentricity (Figure 7), images were captured with a Leica DM5500B widefield microscope, a 63x oil objective, a Hamamatsu ORCA-Flash4.0 sCMOS camera and the Leica Application Suite (LasX) software (Leica Microsystems). All confocal images in the same experiment were acquired using the same laser intensity and gain, and were then processed in Adobe Photoshop (CC2020) where the same image treatment was applied across conditions.

To measure stereocilia length and width in IHC (Figure 2C-D), SEM samples were imaged laterally at 10,000x magnification and with an appropriate tilt (from 0 to 30°) to bring stereocilia parallel to the imaging plane and minimize parallax. To quantify the number of rows in adult IHC and the number of stereocilia in their first row (Figure 2E, F), SEM samples were imaged medially at 5,000x magnification. To measure the length of OHC hair bundle wings (Figure 2G, Figure 2 Supp. 1E), OHC were imaged top down at 5,000x. Stereocilia width was measure at half-length and all measurements were done with the straight-line tool in Fiji.

To quantify GNAI signal intensity in *Gnai1*$^{neo}$*; Gnai3*$^{neo}$ mutants (Figure 5C, Figure 5 Supp. 1A), Z-stack series were acquired at the mid cochlear position. A single Z slice was chosen at the bare zone level, another one at the stereocilia tip level, each based on strongest signal in that compartment. The vertex of the V-shaped hair bundle was used to divide the HC apical surface in two equal halves. In each half (left and right), regions of interest (ROIs) were drawn using the polygon selection tool in Fiji to encompass all

917 signals in that apical compartment, and mean gray values were measured. For each
918 image, background signal was measured and averaged, and subtracted from all
919 measurements in the same image.
920
921 To quantify surface area of the bare zone or total surface area in half-OHC as well as the
922 length of half hair bundles (Figure 5G, Figure 5 Supp. 1C; Figure 6D, H), Z-stack series
923 were acquired at the cochlear base and a single Z slice was selected at apical junction
924 level using ZO1 (Figure 5G, Figure 5 Supp. 1C) or F-actin (Figure 6D, H) as reference.
925 To measure total apical surface area and bundle length in half-OHC, the pericentrin-
926 stained basal body was used to divide the apical surface in two halves (Figure 5G, Figure
927 5 Supp. 1C). The ZO1-positive cell outline along with the dividing line at the basal body
928 level were used as reference to measure surface area with the polygon selection tool in
929 Fiji. To quantify the bare zone surface area (Figure 6D, H), a ROI was drawn around the
930 total apical surface lacking phalloidin (F-actin) signals. The length of the F-actin stained
931 hair bundle was measured using the straight-line tool in Fiji.
932
933 To determine HC eccentricity (Figure 7), the geometrical center of the HC apical surface
934 was determined as the intersection of two orthogonal lines representing the maximal
935 diameter of the cell along the cochlear longitudinal and radial axes. A vector (BB) was
936 drawn from the center to the pericentrin-labeled basal body, and eccentricity was
937 calculated as the ratio of BB length over the cell radius (r) along the same trajectory using
938 F-actin-labeled apical junction as landmark (see Figure 7). To determine cell orientation
939 (Figure 8 and Figure 8 Supp. 1-2), the angle ($\alpha$) separating the longitudinal axis of the
940 organ of Corti from the BB vector was measured with the angle tool in Fiji (see Figure 8).
941 Both right and left cochleae were used and angles were measured so that 0° pointed
942 toward the cochlear base and 90° towards the cochlear periphery (lateral). Eccentricity
943 and angles were measured at the cochlear positions indicated (base ~20%, mid ~50%,
944 apex ~80% of the cochlear length starting from the base).
945
946 **Auditory Brainstem Response (ABR) tests**

947 All tests were performed in a sound-attenuating chamber, and body temperature of the
948 anesthetized animals was maintained at 37°C using a heating pad (FHC Inc.). Animals
949 from all strains except *Atoh1-Cre; Gnao1*$^{flox}$ (Figure 3 Supp. 1B, see below) were
950 anesthetized with a mix of ketamine and xylazine (1 mg and 0.8 mg per 10g of body
951 weight, respectively) and tested using the RZ6 Multi-I/O Processor System coupled to the
952 RA4PA 4-channel Medusa Amplifier (Tucker-Davis Technologies). ABRs were recorded
953 after binaural stimulation in an open field by tone bursts at 8, 16, 32, and in some cases
954 40 kHz generated at 21 stimuli/second, and a waveform for each frequency/dB level was
955 produced by averaging the responses from 512 stimuli. Subdermal needles were used as
956 electrodes, the active electrode inserted at the cranial vertex, the reference electrode
957 under the left ear and the ground electrode at the right thigh.
958 *Atoh1-Cre; Gnao1*$^{flox}$ animals (Figure 3 Supp. 1B) were anesthetized with tribromoethanol
959 (2.5mg per 10g of body weight) and tested with the Smart EP evoked potential system
960 from Intelligent Hearing Systems (IHS). ABR were recorded after single ear stimulation
961 (right ear), using ear tubes speakers (ER3C insert earphones, IHS) delivering tone bursts
962 at 8, 16, and 32 kHz generated at 40 stimuli/second. Electrodes were positioned as
963 previously described except for the ground electrode that was placed at the base of the
964 tail. ABR thresholds were obtained for each frequency by reducing the sound pressure
965 level (SPL) by 5 decibels (dB) between 90 and 20 dB to identify the lowest level at which
966 an ABR waveform could be recognized. We compared waveforms by simultaneously
967 displaying 3 or more dB levels on screen at the same time.
968
969 **Statistical Analyses**
970 All data were plotted in Prism 9 (GraphPad), except for circular diagrams of HC orientation
971 (Figure 8; Figure 8 Supp. 1-2) that were generated with R (4.2.2) and Rstudio
972 (2022.12.0+353).
973
974 All data except for angles in circular diagrams (Figure 8 and Figure 8 Supp. 1-2) were
975 plotted individually. Distribution was framed with 25-75% whisker boxes where exterior
976 lines show the minimum and maximum, the middle line represents the median, and +
977 represents the mean. Potential differences in data distribution between genotypes were

tested for significance using nested (hierarchical) t-test except for ABR thresholds (Figure 3 and Figure 3 Supp. 1) where a 2-way ANOVA with Sidak's multiple comparison post-hoc test was used. Nested t-tests help avoid pseudoreplication by taking into consideration the data structure, here specifically variance in each animal (Eisner, 2021; Krey et al, 2023). OHC half-bundle lengths (Figure 2G, Figure 2 Supp. 1E) were plotted as paired left and right values in the same HC and a potential difference in data variance between genotypes was tested using a F-test. GNAI signal intensity at the OHC bare zone and stereocilia tips (Figure 5C, Figure 5 Supp. 1A) as well as OHC surface area and half-bundle length (Figure 5G, Figure 5 Supp. 1C) were plotted and a simple linear regression curve was calculated and drawn for each pair of datasets. A correlation between variables was addressed with Pearson's correlation test. Exact p-values were indicated on each graph when non-significant ($p>0.05$) and otherwise summarized as follows: $p<0.0001$ ****, $p<0.001$ ***, $p<0.01$**, $p<0.05$*. Details of statistical results for all figures can be found in the Supplementary Data file.

Angle frequency distribution (Figure 8 and Figure 8 Supp. 1-2) was plotted in circular diagrams using the R package dyplr and the coord_polar function of the ggplot2 package to organize data and produce the graphs, respectively. The angle formed by the red line indicates the circular mean and the length of the arc at the end of the red line indicates the mean circular deviation. Both values were obtained using the colstats function in the R circular package. All scripts used in this work will be posted on github.

## ACKNOWLEDGMENTS

We are grateful to Elli Hartig for reading and commenting on the manuscript. We thank Simon Lesbirel for nanopore-based Cas9-targeted sequencing of the *DIO-ptxA* strain. We are grateful to The Jackson Laboratory Genome Engineering Technology and Reproductive Science services for their help with generating the *Gnai2*$^{del}$ and *Gnai3*$^{flox}$ strains, and cryorecovering the *Gnai1*$^{neo}$*; Gnai3*$^{neo}$ and *Gnao1*$^{neo}$ strains, respectively. A.J. was supported by a postdoctoral fellowship from Fondation Pour l'Audition (2018-2020;

FPA RD-2018-3). This work was supported by the National Institute on Deafness and Other Communication Disorders grants R01DC015242 and R01DC018304 (to B.T.).

## AUTHOR CONTRIBUTION

B.T. conceived the study. B.T., A.J and A.L.T designed, performed and analyzed experiments. M.D. provided technical help with mouse colony maintenance, sample processing and genotyping. B. K. wrote the R script to generate the circular histograms. B.E.L and M.V.W. helped generate the *DIO-ptxA* strain using BxB1 recombination technology. B.T supervised the work. B.T. and A.J. wrote the manuscript. B.T. secured funding.

## COMPETETING INTERESTS

The authors declare no competing interest.

## DATA AVAILABILITY

The data in all graphical representations are included in a single Source Data file. Original material used for quantifications and to build figures will be deposited in a publicly accessible repository.

1030 **REFERENCES**

1031


1032 Akturk, A., Day, M. & Tarchini, B. (2022) RGS12 polarizes the GPSM2-GNAI complex to
1033 organize and elongate stereocilia in sensory hair cells. *Sci Adv*, 8(42), eabq2826.

1034 Anniko, M. (1983) Postnatal maturation of cochlear sensory hairs in the mouse. *Anat*
1035 *Embryol (Berl)*, 166(3), 355-68.

1036 Beer-Hammer, S., Lee, S. C., Mauriac, S. A., Leiss, V., Groh, I. A. M., Novakovic, A.,
1037 Piekorz, R. P., Bucher, K., Chen, C., Ni, K., Singer, W., Harasztosi, C., Schimmang, T.,
1038 Zimmermann, U., Pfeffer, K., Birnbaumer, L., Forge, A., Montcouquiol, M., Knipper, M.,
1039 Nurnberg, B. & Ruttiger, L. (2018) Galphai Proteins are Indispensable for Hearing. *Cell*
1040 *Physiol Biochem*, 47(4), 1509-1532.

1041 Bhonker, Y., Abu-Rayyan, A., Ushakov, K., Amir-Zilberstein, L., Shivatzki, S., Yizhar-
1042 Barnea, O., Elkan-Miller, T., Tayeb-Fligelman, E., Kim, S. M., Landau, M., Kanaan, M.,
1043 Chen, P., Matsuzaki, F., Sprinzak, D. & Avraham, K. B. (2016) The GPSM2/LGN GoLoco
1044 motifs are essential for hearing. *Mamm Genome*, 27(1-2), 29-46.

1045 Deans, M. R. (2013) A balance of form and function: planar polarity and development of
1046 the vestibular maculae. *Semin Cell Dev Biol*, 24(5), 490-8.

1047 Denman-Johnson, K. & Forge, A. (1999) Establishment of hair bundle polarity and
1048 orientation in the developing vestibular system of the mouse. *J Neurocytol*, 28(10-11),
1049 821-35.

1050 Doherty, D., Chudley, A. E., Coghlan, G., Ishak, G. E., Innes, A. M., Lemire, E. G., Rogers,
1051 R. C., Mhanni, A. A., Phelps, I. G., Jones, S. J., Zhan, S. H., Fejes, A. P., Shahin, H.,
1052 Kanaan, M., Akay, H., Tekin, M., Consortium, F. C., Triggs-Raine, B. & Zelinski, T. (2012)
1053 GPSM2 mutations cause the brain malformations and hearing loss in Chudley-
1054 McCullough syndrome. *Am J Hum Genet*, 90(6), 1088-93.

1055 Du, Q., Stukenberg, P. T. & Macara, I. G. (2001) A mammalian Partner of inscuteable
1056 binds NuMA and regulates mitotic spindle organization. *Nat Cell Biol*, 3(12), 1069-75.

1057 Eisner, D. A. (2021) Pseudoreplication in physiology: More means less. *J Gen Physiol*,
1058 153(2).

1059 Etournay, R., Lepelletier, L., Boutet de Monvel, J., Michel, V., Cayet, N., Leibovici, M.,
1060 Weil, D., Foucher, I., Hardelin, J. P. & Petit, C. (2010) Cochlear outer hair cells undergo
1061 an apical circumference remodeling constrained by the hair bundle shape. *Development*,
1062 137(8), 1373-83.

1063 Ezan, J., Lasvaux, L., Gezer, A., Novakovic, A., May-Simera, H., Belotti, E., Lhoumeau,
1064 A. C., Birnbaumer, L., Beer-Hammer, S., Borg, J. P., Le Bivic, A., Nurnberg, B., Sans, N.
1065 & Montcouquiol, M. (2013) Primary cilium migration depends on G-protein signalling
1066 control of subapical cytoskeleton. *Nat Cell Biol*, 15(9), 1107-15.

1067 Gilpatrick, T., Lee, I., Graham, J. E., Raimondeau, E., Bowen, R., Heron, A., Downs, B.,
1068 Sukumar, S., Sedlazeck, F. J. & Timp, W. (2020) Targeted nanopore sequencing with
1069 Cas9-guided adapter ligation. *Nat Biotechnol*, 38(4), 433-438.

1070 Gohla, A., Klement, K., Piekorz, R. P., Pexa, K., vom Dahl, S., Spicher, K., Dreval, V.,
1071 Häussinger, D., Birnbaumer, L. & Nürnberg, B. (2007) An obligatory requirement for the
1072 heterotrimeric G protein Gi3 in the antiautophagic action of insulin in the liver. *Proc Natl*
1073 *Acad Sci U S A*, 104(8), 3003-8.

1074 Greene, D., Genomics England Research, C., Pirri, D., Frudd, K., Sackey, E., Al-Owain,
1075 M., Giese, A. P. J., Ramzan, K., Riaz, S., Yamanaka, I., Boeckx, N., Thys, C., Gelb, B.
1076 D., Brennan, P., Hartill, V., Harvengt, J., Kosho, T., Mansour, S., Masuno, M., Ohata, T.,
1077 Stewart, H., Taibah, K., Turner, C. L. S., Imtiaz, F., Riazuddin, S., Morisaki, T.,
1078 Ostergaard, P., Loeys, B. L., Morisaki, H., Ahmed, Z. M., Birdsey, G. M., Freson, K.,
1079 Mumford, A. & Turro, E. (2023) Genetic association analysis of 77,539 genomes reveals
1080 rare disease etiologies. *Nat Med*.

1081 Hebert, J. M. & McConnell, S. K. (2000) Targeting of cre to the Foxg1 (BF-1) locus
1082 mediates loxP recombination in the telencephalon and other developing head structures.
1083 *Dev Biol*, 222(2), 296-306.

1084 Jarysta, A. & Tarchini, B. (2021) Multiple PDZ domain protein maintains patterning of the
1085 apical cytoskeleton in sensory hair cells. *Development*, 148(14).

1086 Jia, S., Ratzan, E. M., Goodrich, E. J., Abrar, R., Heiland, L., Tarchini, B. & Deans, M. R.
1087 (2023) The dark kinase STK32A regulates hair cell planar polarity opposite of EMX2 in
1088 the developing mouse inner ear. *Elife*, 12.

1089 Jiang, M., Gold, M. S., Boulay, G., Spicher, K., Peyton, M., Brabet, P., Srinivasan, Y.,
1090 Rudolph, U., Ellison, G. & Birnbaumer, L. (1998) Multiple neurological abnormalities in
1091 mice deficient in the G protein Go. *Proc Natl Acad Sci U S A*, 95(6), 3269-74.

1092 Jiang, M., Spicher, K., Boulay, G., Martin-Requero, A., Dye, C. A., Rudolph, U. &
1093 Birnbaumer, L. (2002) Mouse gene knockout and knockin strategies in application to
1094 alpha subunits of Gi/Go family of G proteins. *Methods Enzymol*, 344, 277-98.

1095 Jiang, T., Kindt, K. & Wu, D. K. (2017) Transcription factor Emx2 controls stereociliary
1096 bundle orientation of sensory hair cells. *Elife*, 6.

1097 Jones, C., Roper, V. C., Foucher, I., Qian, D., Banizs, B., Petit, C., Yoder, B. K. & Chen,
1098 P. (2008) Ciliary proteins link basal body polarization to planar cell polarity regulation. *Nat*
1099 *Genet*, 40(1), 69-77.

1100 Kindt, K. S., Akturk, A., Jarysta, A., Day, M., Beirl, A., Flonard, M. & Tarchini, B. (2021)
1101 EMX2-GPR156-Galphai reverses hair cell orientation in mechanosensory epithelia. *Nat*
1102 *Commun*, 12(1), 2861.

1103 Krey, J. F., Chatterjee, P., Halford, J., Cunningham, C. L., Perrin, B. J. & Barr-Gillespie,
1104 P. G. (2023) Control of stereocilia length during development of hair bundles. *PLoS Biol*,
1105 21(4), e3001964.

1106 Locht, C., Coutte, L. & Mielcarek, N. (2011) The ins and outs of pertussis toxin. *FEBS J*,
1107 278(23), 4668-82.

1108 Low, B. E., Hosur, V., Lesbirel, S. & Wiles, M. V. (2022) Efficient targeted transgenesis
1109 of large donor DNA into multiple mouse genetic backgrounds using bacteriophage Bxb1
1110 integrase. *Sci Rep*, 12(1), 5424.

1111 Matei, V., Pauley, S., Kaing, S., Rowitch, D., Beisel, K. W., Morris, K., Feng, F., Jones,
1112 K., Lee, J. & Fritzsch, B. (2005) Smaller inner ear sensory epithelia in Neurog 1 null mice
1113 are related to earlier hair cell cycle exit. *Dev Dyn*, 234(3), 633-50.

1114 Mauriac, S. A., Hien, Y. E., Bird, J. E., Carvalho, S. D., Peyroutou, R., Lee, S. C., Moreau,
1115 M. M., Blanc, J. M., Geyser, A., Medina, C., Thoumine, O., Beer-Hammer, S., Friedman,
1116 T. B., Ruttiger, L., Forge, A., Nurnberg, B., Sans, N. & Montcouquiol, M. (2017) Defective
1117 Gpsm2/Galphai3 signalling disrupts stereocilia development and growth cone actin
1118 dynamics in Chudley-McCullough syndrome. *Nat Commun*, 8, 14907.

1119 May-Simera, H. L., Petralia, R. S., Montcouquiol, M., Wang, Y. X., Szarama, K. B., Liu,
1120 Y., Lin, W., Deans, M. R., Pazour, G. J. & Kelley, M. W. (2015) Ciliary proteins Bbs8 and
1121 Ift20 promote planar cell polarity in the cochlea. *Development*, 142(3), 555-66.

1122 Mbiene, J. P. & Sans, A. (1986) Differentiation and maturation of the sensory hair bundles
1123 in the fetal and postnatal vestibular receptors of the mouse: a scanning electron
1124 microscopy study. *J Comp Neurol*, 254(2), 271-8.

1125 Montcouquiol, M. & Kelley, M. W. (2019) Development and Patterning of the Cochlea:
1126 From Convergent Extension to Planar Polarity. *Cold Spring Harb Perspect Med*.

1127 Plummer, N. W., Spicher, K., Malphurs, J., Akiyama, H., Abramowitz, J., Nürnberg, B. &
1128 Birnbaumer, L. (2012) Development of the mammalian axial skeleton requires signaling

1129 through the Gα(i) subfamily of heterotrimeric G proteins. *Proc Natl Acad Sci U S A*,
1130 109(52), 21366-71.

1131 Qin, W., Dion, S. L., Kutny, P. M., Zhang, Y., Cheng, A. W., Jillette, N. L., Malhotra, A.,
1132 Geurts, A. M., Chen, Y. G. & Wang, H. (2015) Efficient CRISPR/Cas9-Mediated Genome
1133 Editing in Mice by Zygote Electroporation of Nuclease. *Genetics*, 200(2), 423-30.

1134 Ramzan, M., Bozan, N., Seyhan, S., Zafeer, M. F., Ayral, A., Duman, D., Bademci, G. &
1135 Tekin, M. (2023) Novel GPR156 variants confirm its role in moderate sensorineural
1136 hearing loss. *Sci Rep*, 13(1), 17010.

1137 Regard, J. B., Kataoka, H., Cano, D. A., Camerer, E., Yin, L., Zheng, Y. W., Scanlan, T.
1138 S., Hebrok, M. & Coughlin, S. R. (2007) Probing cell type-specific functions of Gi in vivo
1139 identifies GPCR regulators of insulin secretion. *J Clin Invest*, 117(12), 4034-43.

1140 Schaefer, M., Petronczki, M., Dorner, D., Forte, M. & Knoblich, J. A. (2001) Heterotrimeric
1141 G proteins direct two modes of asymmetric cell division in the Drosophila nervous system.
1142 *Cell*, 107(2), 183-94.

1143 Schaefer, M., Shevchenko, A., Shevchenko, A. & Knoblich, J. A. (2000) A protein complex
1144 containing Inscuteable and the Galpha-binding protein Pins orients asymmetric cell
1145 divisions in Drosophila. *Curr Biol*, 10(7), 353-62.

1146 Schnutgen, F., Doerflinger, N., Calleja, C., Wendling, O., Chambon, P. & Ghyselinck, N.
1147 B. (2003) A directional strategy for monitoring Cre-mediated recombination at the cellular
1148 level in the mouse. *Nat Biotechnol*, 21(5), 562-5.

1149 Siletti, K., Tarchini, B. & Hudspeth, A. J. (2017) Daple coordinates organ-wide and cell-
1150 intrinsic polarity to pattern inner-ear hair bundles. *Proc Natl Acad Sci U S A*, 114(52),
1151 E11170-E11179.

1152 Sipe, C. W. & Lu, X. (2011) Kif3a regulates planar polarization of auditory hair cells
1153 through both ciliary and non-ciliary mechanisms. *Development*, 138(16), 3441-9.

1154 Tadenev, A. L. D., Akturk, A., Devanney, N., Mathur, P. D., Clark, A. M., Yang, J. &
1155 Tarchini, B. (2019) GPSM2-GNAI Specifies the Tallest Stereocilia and Defines Hair
1156 Bundle Row Identity. *Curr Biol*, 29(6), 921-934 e4.

1157 Tarchini, B. (2021) A Reversal in Hair Cell Orientation Organizes Both the Auditory and
1158 Vestibular Organs. *Front Neurosci*, 15, 695914.

1159 Tarchini, B., Jolicoeur, C. & Cayouette, M. (2013) A molecular blueprint at the apical
1160 surface establishes planar asymmetry in cochlear hair cells. *Dev Cell*, 27(1), 88-102.

1161 Tarchini, B. & Lu, X. (2019) New insights into regulation and function of planar polarity in
1162 the inner ear. *Neurosci Lett*, 709, 134373.

1163 Tarchini, B., Tadenev, A. L., Devanney, N. & Cayouette, M. (2016) A link between planar
1164 polarity and staircase-like bundle architecture in hair cells. *Development*, 143(21), 3926-
1165 3932.

1166 Tilney, L. G., Tilney, M. S. & DeRosier, D. J. (1992) Actin filaments, stereocilia, and hair
1167 cells: how cells count and measure. *Annu Rev Cell Biol*, 8, 257-74.

1168 Tona, Y. & Wu, D. K. (2020) Live imaging of hair bundle polarity acquisition demonstrates
1169 a critical timeline for transcription factor Emx2. *Elife*, 9.

1170 Walsh, T., Shahin, H., Elkan-Miller, T., Lee, M. K., Thornton, A. M., Roeb, W., Abu
1171 Rayyan, A., Loulus, S., Avraham, K. B., King, M. C. & Kanaan, M. (2010) Whole exome
1172 sequencing and homozygosity mapping identify mutation in the cell polarity protein
1173 GPSM2 as the cause of nonsyndromic hearing loss DFNB82. *Am J Hum Genet*, 87(1),
1174 90-4.

1175 Watkins, L. R. & Orlandi, C. (2021) In vitro profiling of orphan G protein coupled receptor
1176 (GPCR) constitutive activity. *Br J Pharmacol*, 178(15), 2963-2975.

1177 Webb, S. W., Grillet, N., Andrade, L. R., Xiong, W., Swarthout, L., Della Santina, C. C.,
1178 Kachar, B. & Muller, U. (2011) Regulation of PCDH15 function in mechanosensory hair
1179 cells by alternative splicing of the cytoplasmic domain. *Development*, 138(8), 1607-17.

1180 Woodard, G. E., Huang, N. N., Cho, H., Miki, T., Tall, G. G. & Kehrl, J. H. (2010) Ric-8A
1181 and Gi alpha recruit LGN, NuMA, and dynein to the cell cortex to help orient the mitotic
1182 spindle. *Mol Cell Biol*, 30(14), 3519-30.

1183

1184

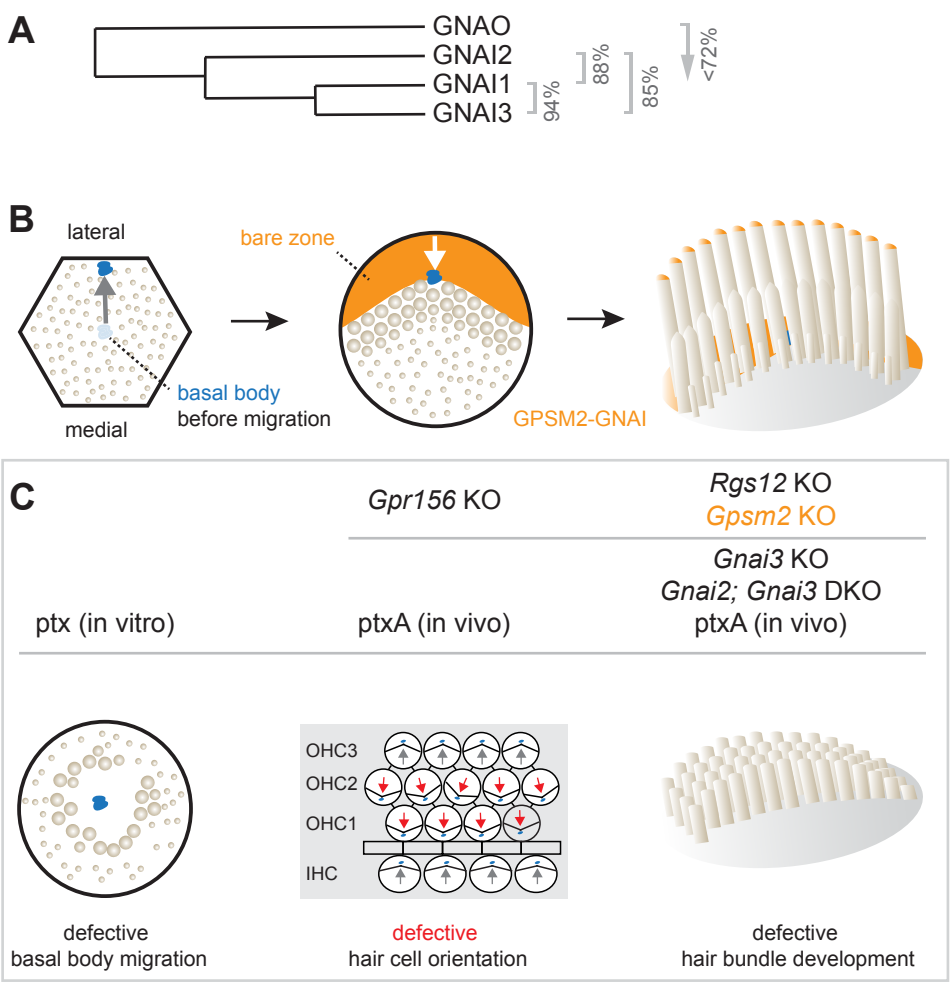


**Figure 1. Summary of GNAI-related functions proposed previously in hair cells. A)** Phylogenetic tree of GNAI/O proteins with percent amino acid identity (mouse). **B)** Apical HC differentiation from symmetry breaking to hair bundle development. The distribution of the GPSM2-GNAI complex at the bare zone and stereocilia tips is indicated in orange. Arrows indicate off-center (left) and then inward (middle) movements of the basal body. **C)** Defects observed with pertussis toxin (ptx) or when inactivating GNAI proteins. Defective off-center migration of the basal body and inverted OHC1-2 were only observed with ptx, respectively in cochlear explants (in vitro) and by expressing the ptx catalytic subunit (ptxA) in vivo. Mouse knock-out (KO)s of *Gnai* genes were to date only reported to affect hair bundle morphogenesis. Known GNAI regulators that produce similar defects when inactivated are indicated on top for each type of defect. DKO, double KO.

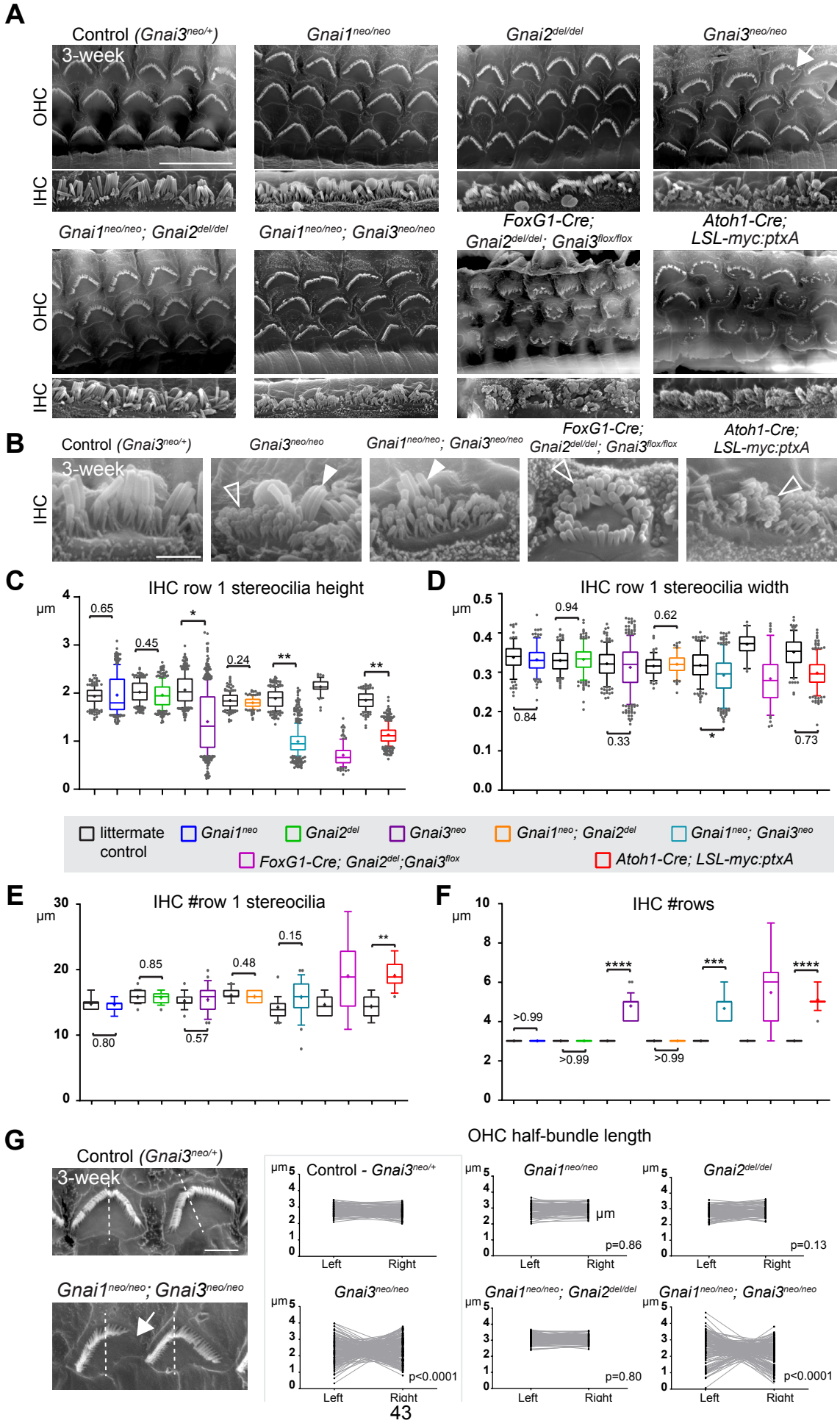
A
Control (Gnai3neo/+)
3-week
Gnai1neo/neo
Gnai2del/del
Gnai3neo/neo
OHC
IHC
Gnai1neo/neo; Gnai2del/del
Gnai1neo/neo; Gnai3neo/neo
FoxG1-Cre; Gnai2del/del; Gnai3flox/flox
Atoh1-Cre; LSL-myc:ptxA
B
C
IHC row 1 stereocilia height
µm
0.65
0.45
*
0.24
**
**
D
IHC row 1 stereocilia width
0.94
0.62
0.84
0.33
*
0.73
littermate control
Gnai1neo
Gnai2del
Gnai3neo
Gnai1neo; Gnai2del
Gnai1neo; Gnai3neo
FoxG1-Cre; Gnai2del;Gnai3flox
Atoh1-Cre; LSL-myc:ptxA
E
IHC #row 1 stereocilia
0.85
0.48
0.15
**
0.80
0.57
F
IHC #rows
>0.99
****
>0.99
>0.99
***
****
G
OHC half-bundle length
Control - Gnai3neo/+
Left
Right
p=0.86
p=0.13
p<0.0001
p=0.80
p<0.0001

**Figure 2. Individual GNAI proteins make different contributions to hair bundle development. A-B)** SEM images of representative OHC (A) and IHC (B) in 3-week old animals at the cochlear mid. *Gnai1*$^{neo}$, *Gnai2*$^{del}$, and *Gnai1*$^{neo}$*; Gnai2*$^{del}$ mutants show apparently normal hair bundles in both HC types. In contrast, *Gnai3*$^{neo}$ and *Gnai1*$^{neo}$*; Gnai3*$^{neo}$ mutants show defects in both HC types, including truncated hair bundles in OHC (arrow), as well as supernumerary rows of stunted (hollow arrowheads) or variable height stereocilia (full arrowheads) in IHC. In addition, in *FoxG1-Cre; Gnai2*$^{del}$*; Gnai3*$^{flox}$ and *Atoh1-Cre; LSL-myc:ptxA* mutants, OHC1-2s are severely misoriented. **C-F)** Quantification of various hair bundle features in 3-week old IHC at the cochlear mid. Each mutant strain is compared to littermate controls (in black; exact genotypes detailed in Source Data file). At least 3 animals, 17 IHC and 108 stereocilia are represented per condition, except for *FoxG1-Cre; Gnai2*$^{del}$*; Gnai3*$^{flox}$ where we could only obtain a single adult animal due to postnatal lethality. Nested (hierarchical) t-test sorted by animal; $p<0.0001$****, $p<0.001$***, $p<0.01$**, $p<0.05$*; non-significant p-values are indicated. Detailed cohort sizes and statistics can be found in Source Data file. **G)** SEM images of representative OHC showing a truncated hair bundle (arrow). Lengths of the left and right wing of the hair bundle were measured and plotted as paired values for the same OHC. A littermate control graph is only shown for *Gnai3* mutants (*Gnai3*$^{neo/+}$ controls). Littermate control graphs for the other mutants can be found in Fig. 2 Supp. 1G. p-values are for a F-test of variance of pooled left and right wing lengths compared to littermate controls. At least 3 animals and 88 OHC are represented per genotype. Only *Gnai3* and *Gnai1*; Gnai3 mutants show truncated hair bundles and a significant p value ($p<0.05$). Scale bars are 10μm (A) and 2μm (B, G). OHC, outer hair cell; IHC, inner hair cell.

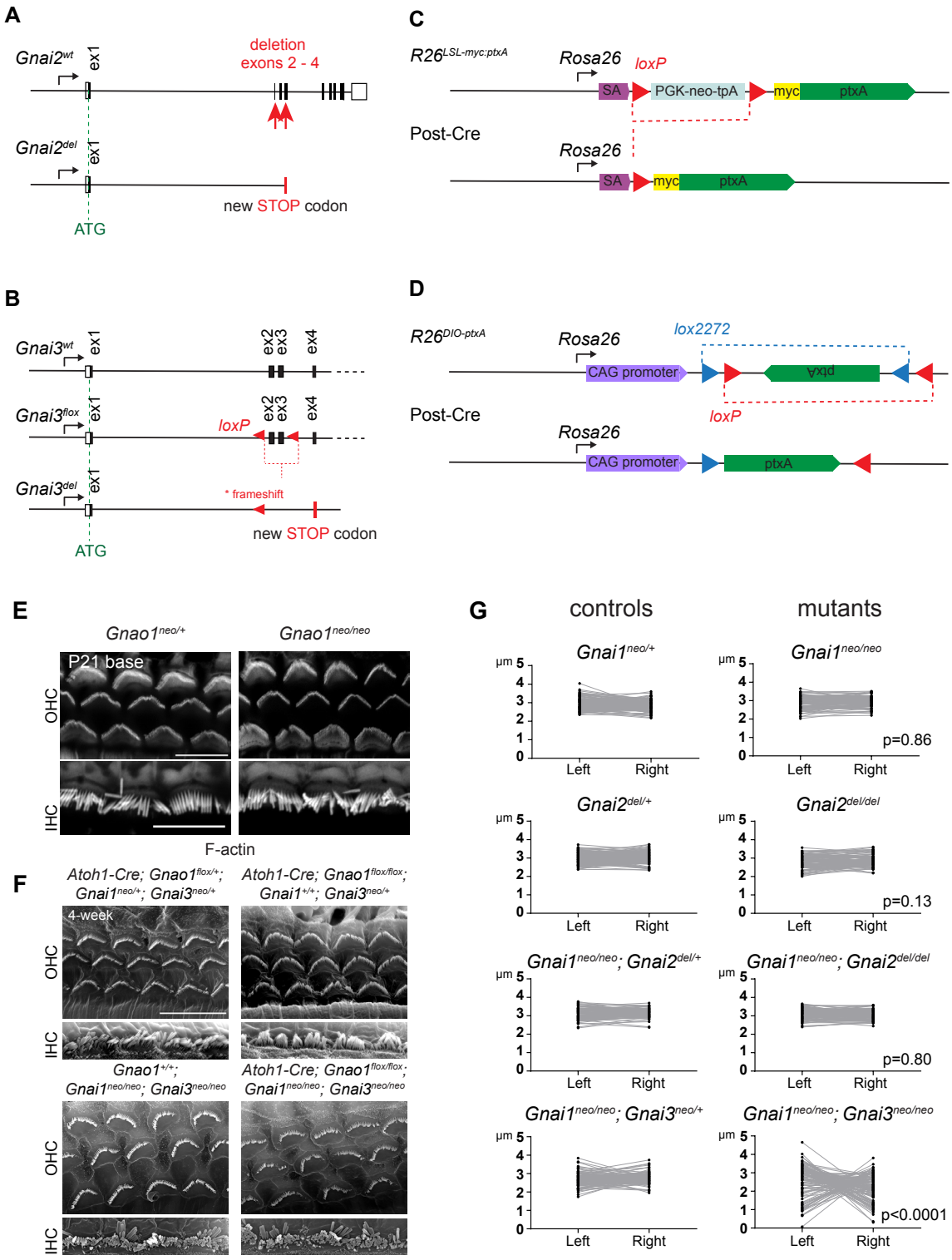


**Figure 2 Supplement 1. A-D)** New mouse strains generated in this study are *Gnai2*$^{del}$ (A), *Gnai3*$^{flox}$ (B) and *R26*$^{DIO\text{-}ptxA}$ (D; see Methods for details). *R26*$^{LSL\text{-}myc:ptxA}$ was published previously and is used in this study as well (C). **E-F)** Loss of GNAO has no obvious impact on apical HC morphology or HC orientation. Representative confocal images of phalloidin-stained *Gnao1* constitutive mutants at P21 (E; *Gnao1*$^{neo}$) and scanning electron microscopy images of conditional *Gnao1* inactivation in the *Gnai1; Gnai3* double mutant background (F; *Gnao1*$^{flox}$). In F, top panels compare control (left) and conditional

*Gnao1* inactivation (right) when GNAI1 and GNAI3 function is preserved. Bottom panels compare control (left) and conditional *Gnao1* inactivation (right) when GNAI1 and GNAI3 are inactivated. Note how HC-specific inactivation of GNAO using the *Atoh1-Cre* driver does not obviously enhance defects observed in *Gnai1; Gnai3* double mutants (F, bottom). **G)** Graphs showing the length of the left and right wing of 3-week-old OHC hair bundles paired by cell. Graphs for control littermates that were omitted in Fig. 2G are added here (left) next to repeated mutant graphs (right). p-values are for a F-test of variance of pooled left and right wing lengths compared to littermate controls. At least 3 animals and 88 OHC are represented per genotype. Only *Gnai3*$^{neo}$ (Fig. 2G) and *Gnai1*$^{neo}$; *Gnai3*$^{neo}$ mutants show truncated hair bundles and a significant p value ($p<0.05$).

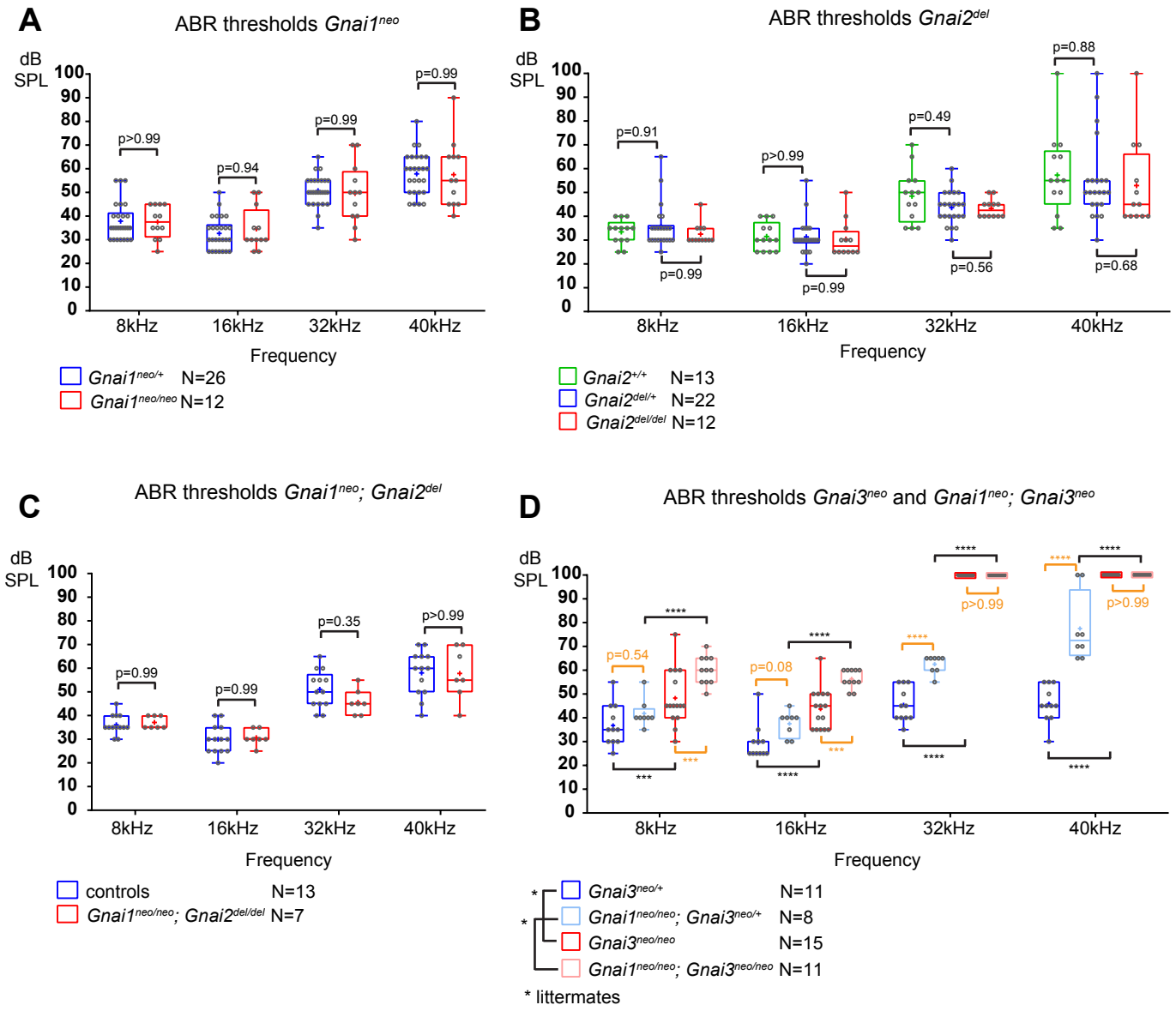


**Figure 3. Loss of GNAI3 leads to hearing loss most severe at high frequencies. A-D)** ABR thresholds at 8, 16, 32, and 40 kHz for *Gnai1*$^{neo}$ (A), *Gnai2*$^{del}$ (B), *Gnai1*$^{neo}$*; Gnai2*$^{del}$ (C), and *Gnai3*$^{neo}$ and *Gnai1*$^{neo}$*; Gnai3*$^{neo}$ (D) mutants tested between P21 and P29. Boxplots are framed with 25-75% whisker boxes where exterior lines show the minimum and maximum values, the middle line represents the median, and + represent the mean. A plotted value of 100 dB indicates animals that did not respond to 90 dB stimuli. In (C), controls are a pool of *Gnai1*$^{+/+}$*; Gnai2*$^{del/+}$, *Gnai1*$^{neo/+}$*; Gnai2*$^{+/+}$ and *Gnai1*$^{neo/+}$*; Gnai2*$^{del/+}$ animals. N indicates the number of animals of both sexes tested. Two-way ANOVA with Sidak's multiple comparison. p<0.0001****, p<0.001***; non-significant p-values are indicated. p-values in orange were obtained comparing non-littermate animals and suggest possibly raised thresholds when GNAI1 is inactivated in addition to GNAI3, or due to a difference in genetic background (see text). kHz, kiloHertz, dB SPL, decibel sound pressure level.

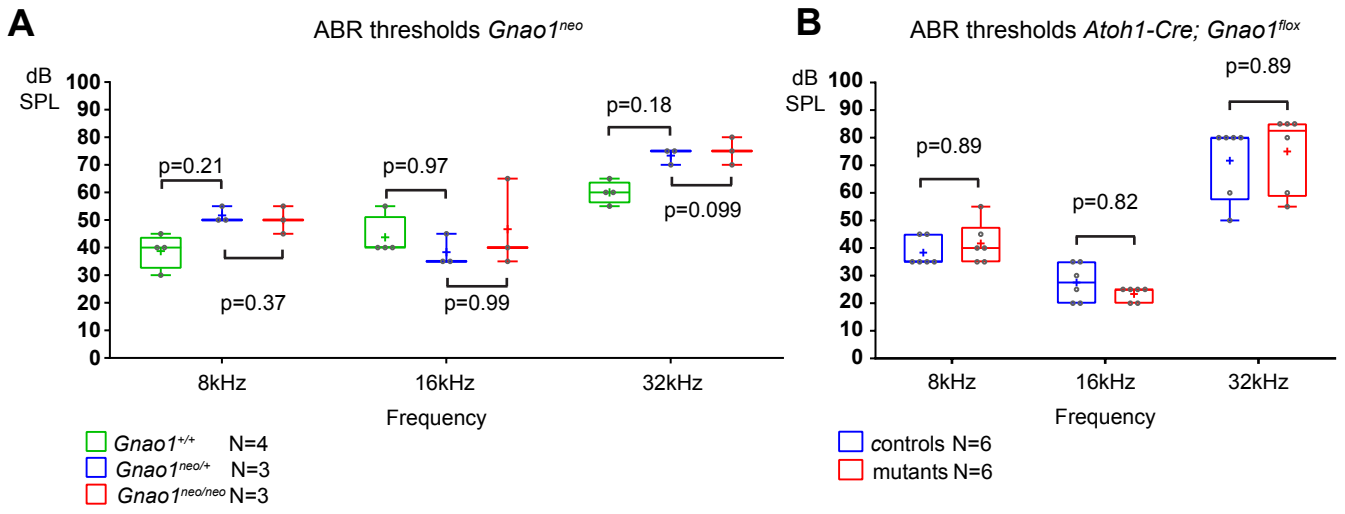


**Figure 3 Supplement 1. A-B)** ABR thresholds at 8, 16, 32 kHz for constitutive *Gnao1* (A) and conditional *Atoh1-Cre; Gnao1*$^{flox/flox}$ (B) mutants tested between P20 and P25. Boxplots are framed with 25-75% whisker boxes where exterior lines show the minimum and maximum values, the middle line represents the median, and + represent the mean. N indicates the number of animals tested. In (B), because the original animal cohort was established to test whether the loss of GNAO could enhance defects in *Gnai1; Gnai3* double mutants (see Fig. 2 Supp. 1F), controls include the following genotypes: *Atoh1-Cre; Gnao1*$^{flox/+}$, *Gnao1*$^{flox/flox}$, *Gnai1*$^{neo/+}$*; Gnai3*$^{neo/+}$, *Gnai1*$^{neo/+}$, *Atoh1-Cre; Gnao1*$^{flox/+}$*; Gnai1*$^{neo/neo}$*; Gnai3*$^{neo/+}$ and *Gnai1*$^{neo/neo}$*; Gnai3*$^{neo/+}$ where other alleles are wild-type. Mutants include the following: *Atoh1-Cre; Gnao1*$^{flox/flox}$; *Gnai3*$^{neo/+}$ and *Atoh1-Cre; Gnao1*$^{flox/flox}$*; Gnai1*$^{neo/neo}$*; Gnai3*$^{neo/+}$ where other alleles are wild-type. Cohort details can be found in Source Data file. Two-way ANOVA with Sidak's multiple comparison. non-significant p-values are indicated. kHz, kiloHertz, dB SPL, decibel sound pressure level.

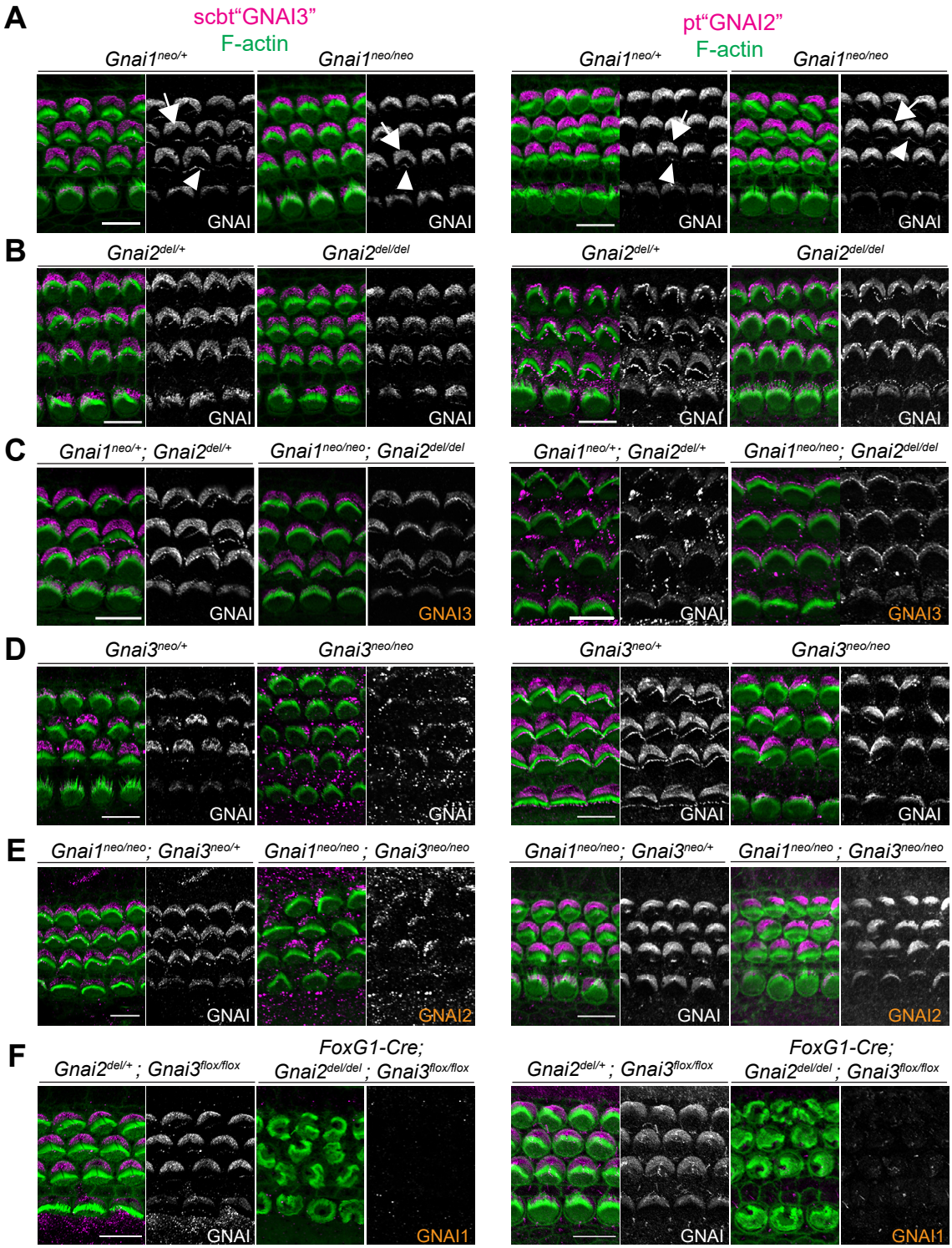


**Figure 4. Systematic immunolabeling of GNAI proteins in *Gnai* mutant strains. A-F)** Two different antibodies (scbt"GNAI3" and pt"GNAI2") were used to label the auditory epithelium at P0-P3. GNAI proteins were detected at the bare zone (arrows) and at stereocilia tips (arrowheads). Neither antibody is specific for its protein target, as scbt"GNAI3" is able to detect GNAI2 (E) and pt"GNAI2" is able to detect GNAI3 (C). Note how no apical GNAI signal is visible with either antibody in *Gnai2; Gnai3* double mutants (F), showing that GNAI1 is not enriched apically in HC (see Fig. 4 Supp. 1A-B for evidence that pt"GNAI2" detects GNAI1). When the identity of the GNAI protein detected is unambiguous based on genotype, it is made explicit in orange. Scale bars are 10µm.

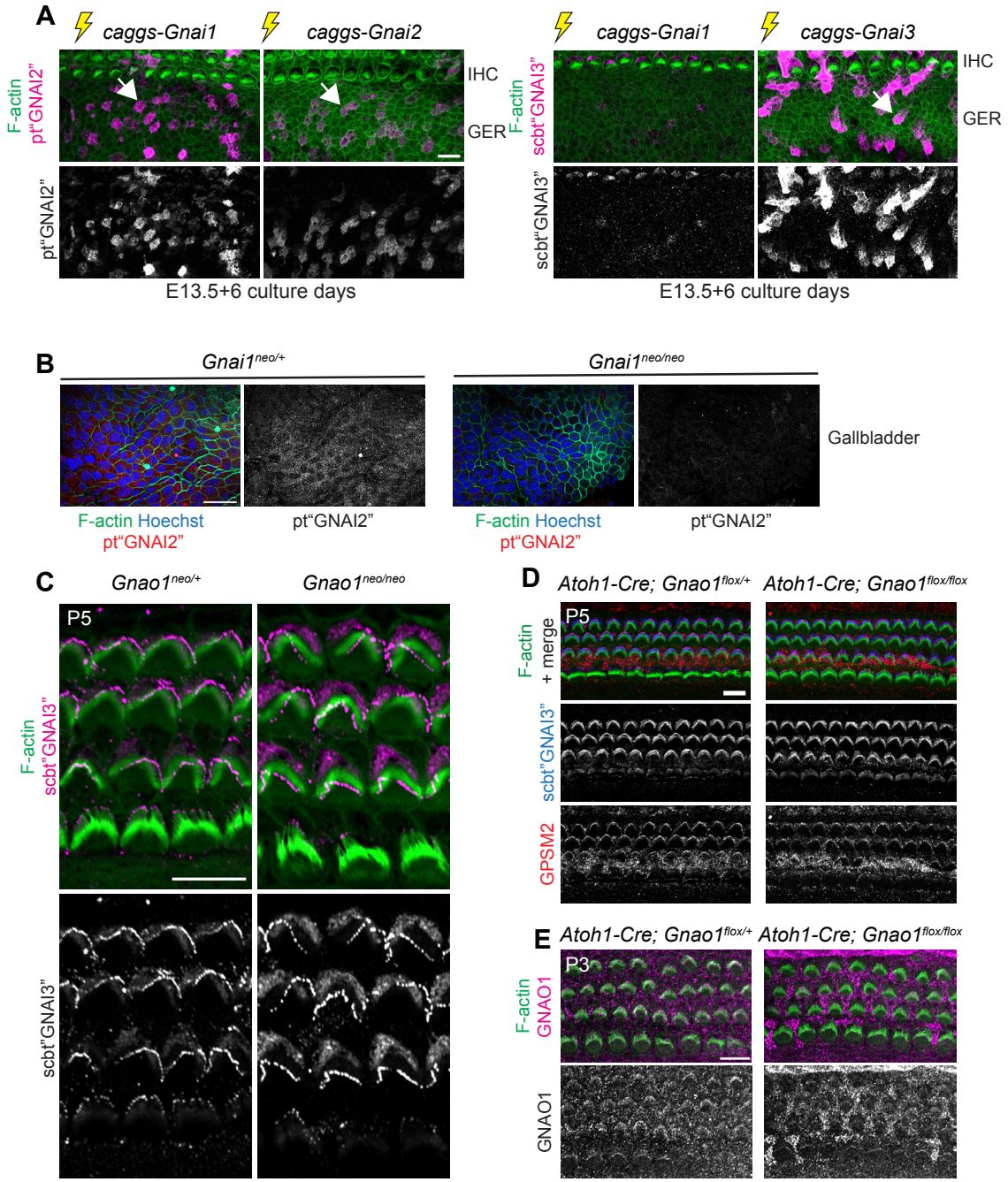


**Figure 4 Supplement 1. GNAI1 detection by Proteintech GNAI2 antibody, GNAI protein distribution in *Gnao1* mutants and lack of evidence for GNAO enrichment at the hair cell apex.** **A)** Cochlear explants electroporated at E13.5 with the Gnai constructs indicated and cultured for 6 days before immunolabeling with Proteintech (pt"GNAI2"; left) or Santa Cruz Biotechnology (scbt"GNAI3"; right) GNAI antibodies (maximum projections). pt"GNAI2" efficiently detects ectopically expressed GNAI1 (and GNAI2, as expected), but scbt"GNAI3" only weakly detects GNAI1 (and efficiently detects GNAI3, as expected). The greater epithelial ridge (GER) is imaged with IHC on top. Caggs: CMV early enhancer/beta-actin promoter expression vector. Results are representative of 3 independent explants. **B)** pt"GNAI2" immunolabeling of the adult gallbladder epithelium (maximum projection) where specific *Gnai1* expression was reported in the *Gnai1*$^{tm1a(EUCOMM)Wtsi}$ mouse strain (International Mouse Phenotyping Consortium; mousephenotype.org). Apical signals are reduced in *Gnai1* mutants, confirming that the

pt”GNAI2” antibody can detect endogenous GNAI1. **C-D)** GNAI (scbt”GNAI3” antibody; see Fig. 4) immunolabeling in P5 *Gnao1* constitutive (C) and *Atoh1-Cre; Gnao1*$^{flox}$ conditional (D) mutants at the cochlear base. Enrichment of GNAI (C-D) and GPSM2 (D) at the bare zone and stereocilia tips is unchanged in absence of GNAO. **E)** GNAO immunolabeling at the P3 cochlear mid produces signals that are unspecific since they are unchanged in conditional *Gnao1* mutants. Scale bars are 10μm (A, C-E) and 25μm (B).

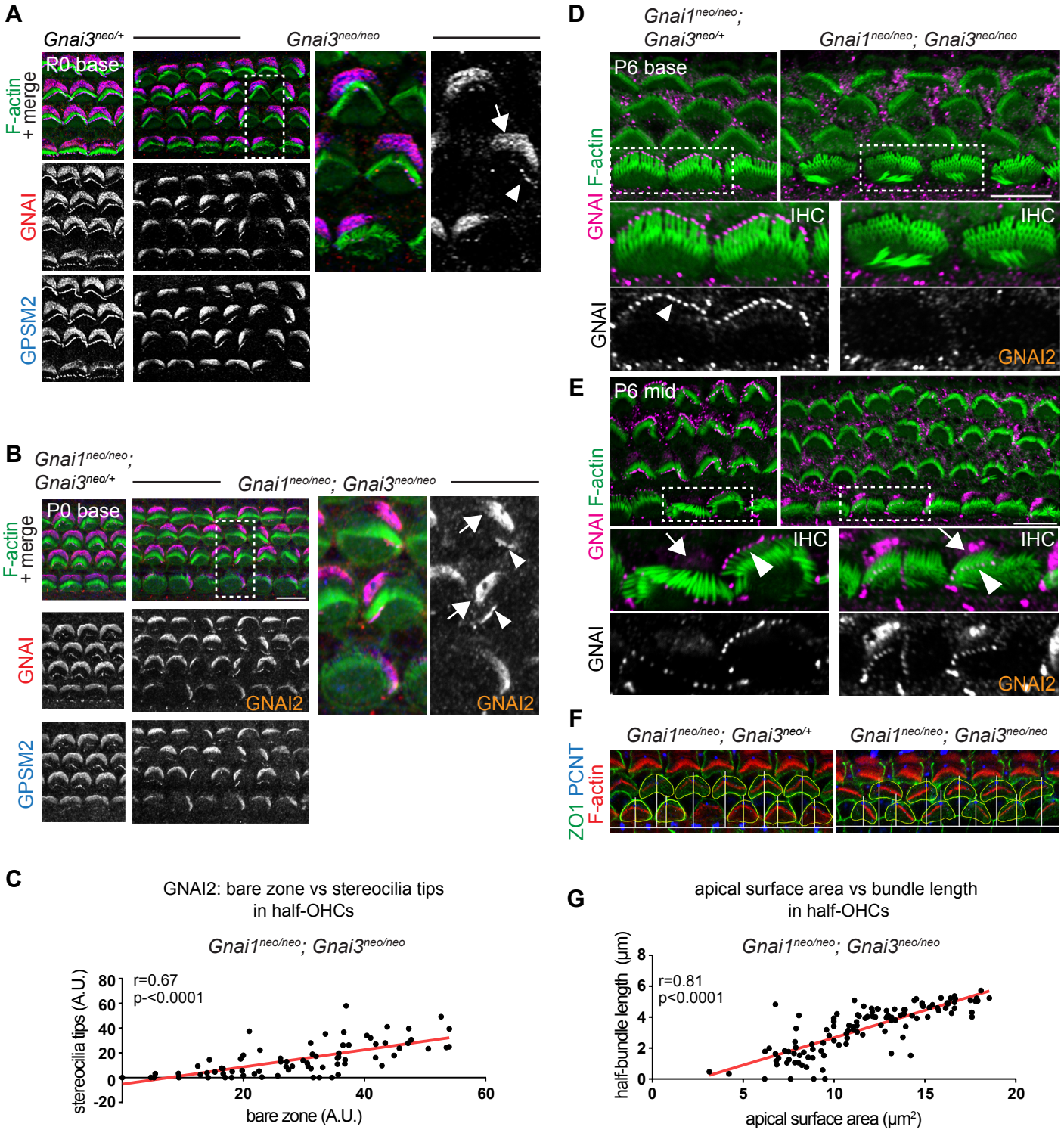


**Figure 5. GNAI2 only partially rescues loss of GNAI3 in individual postnatal hair cells. A-B)** GNAI (pt"GNAI2" antibody; see Fig. 4) and GPSM2 co-immunolabeling in P0 *Gnai3*$^{neo}$ (A) and *Gnai1*$^{neo}$*; Gnai3*$^{neo}$ (B) animals at the cochlear base. Boxed regions are magnified on the right. In both mutants, incomplete GNAI patterns are observed at the bare zone (arrow) and stereocilia tips (arrowheads). Remaining GNAI signals must reflect GNAI2 in (B). **C)** Correlation plot of GNAI signal intensity at the bare zone and tips in half-OHC at the P2 cochlear mid. Presence or absence of GNAI is remarkably correlated spatially between bare zone and tips in the same half-OHC. N=3 animals, n=37 OHC,

Pearson correlation with best fit (red line; plot for control littermates can be found in Fig. 5 Supp. 1A). **D-E)** GNAI (pt"GNAI2" antibody) immunolabeling in P6 *Gnai1*$^{neo}$*; Gnai3*$^{neo}$ animals. Boxed IHC regions are magnified below. Loss of GNAI2 progresses with HC differentiation, with largely absent IHC signals at the P6 cochlear base (D) but partial rescue on one side of the cell at the P6 mid (E), as observed at the cochlear base at P0 (A-B). **F)** ZO1 (apical junctions) and pericentrin (PCNT; basal body) immunolabeling in P8 OHC (maximum projection). The position of the basal body is used to determine the vertex (middle) of the original hair bundle and to draw a radial line separating each OHC into two halves. **G)** The length of each hair bundle wing (y axis) is graphed in relation to the corresponding apical surface area (x axis) in the same half-OHC. Truncated OHC wings correlate with reduced apical membrane area on the same side. N=3 animals, n=58 OHC, Pearson correlation with best fit (red line; plot for control littermates can be found in Fig. 5 Supp. 1C). A.U., arbitrary unit. Scale bars are 10μm.

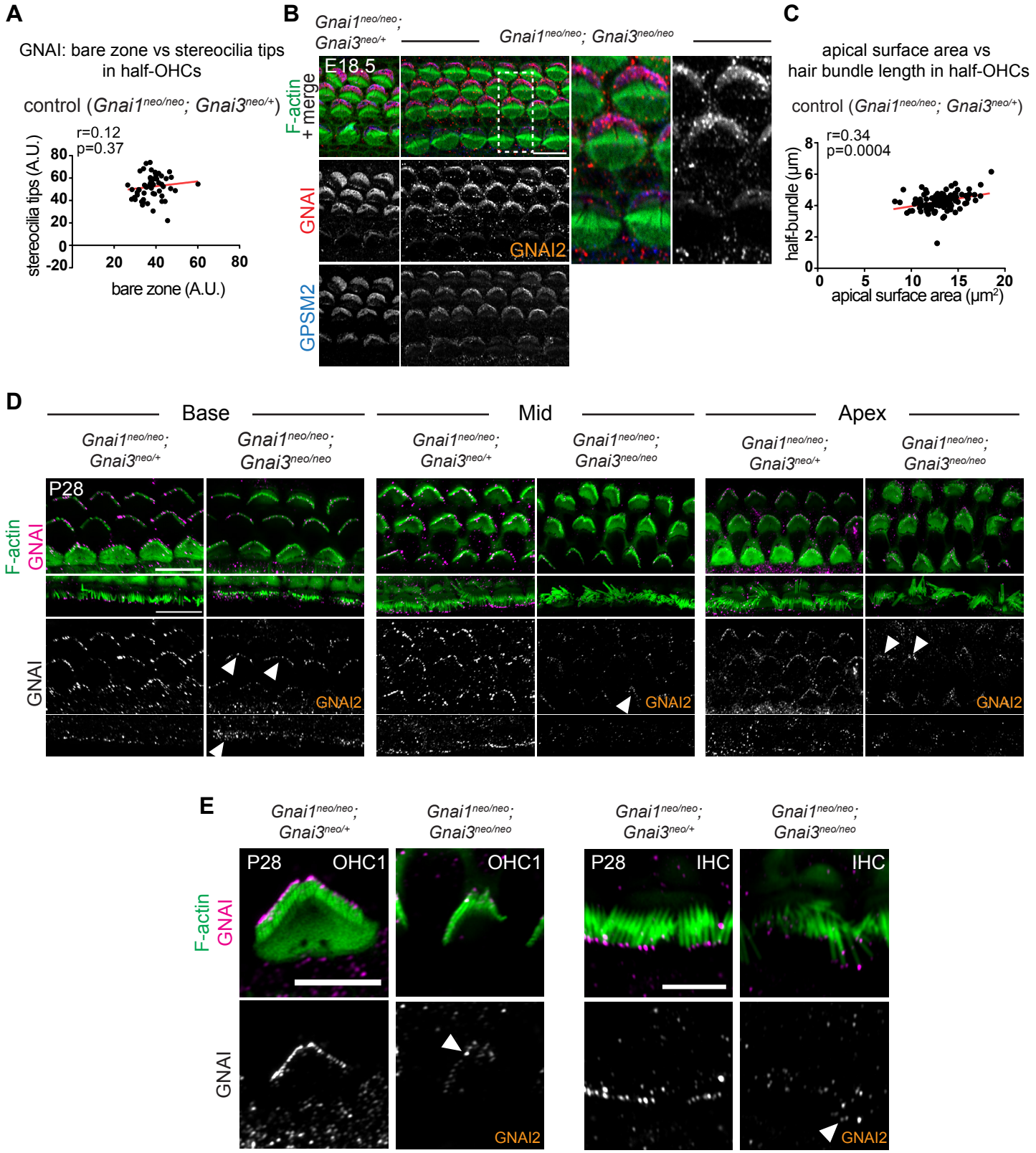


**Figure 5 Supplement 1. GNAI2 fully rescues loss of GNAI3 at embryonic stages and is still detected in low amounts at stereocilia tips in adult hair cells lacking GNAI3. A)** Control correlation plot for *Gnai1; Gnai3* double mutants in Fig. 5C. GNAI signal intensity at the bare zone and stereocilia tips in control half-HC at the P2 cochlear base. N=3 animals, n=40 OHC, Pearson correlation with best fit (red line). The graph shows relatively uniform GNAI enrichment in each sub-cellular compartment, unlike in *Gnai1; Gnai3* double mutants (Fig. 5C). **B)** GNAI (pt"GNAI2" antibody; see Fig. 4) and GPSM2

co-immunolabeling at the E18.5 5 cochlear base. As sole remaining GNAI, GNAI2 can still encompass the entire bare zone in *Gnai1; Gnai3* double mutants and no obvious hair bundle defects are observed, unlike at P0 (Fig. 5A-B). The boxed region is magnified to the right. **C)** Control correlation plot for *Gnai1; Gnai3* double mutants in Fig. 5G. The position of the basal body was used to determine the vertex (middle) of the hair bundle and to draw a radial line separating each OHC into two halves. The length of each hair bundle wing (y axis) is graphed in relation to the corresponding apical surface area (x axis) in the same half-OHC. The plot shows relatively uniform wing lengths and half apical areas in littermate controls, unlike in *Gnai1; Gnai3* double mutants (Fig. 5G). N=3 animals, n=52 OHC, Pearson correlation with best fit (red line). **D-E)** GNAI (pt"GNAI2" antibody; see Fig. 4) immunolabeling in P28 adults (maximum projections). As sole remaining GNAI, GNAI2 can still be detected at low levels at stereocilia tips in *Gnai1; Gnai3* double mutants at the cochlear base, mid and apex (arrowheads). E shows higher magnification views of a single OHC1 (left) and IHC (right) at the cochlear mid. A.U., arbitrary unit. Scale bars are 10μm (B, D) and 5 μm (E).

## E17.5

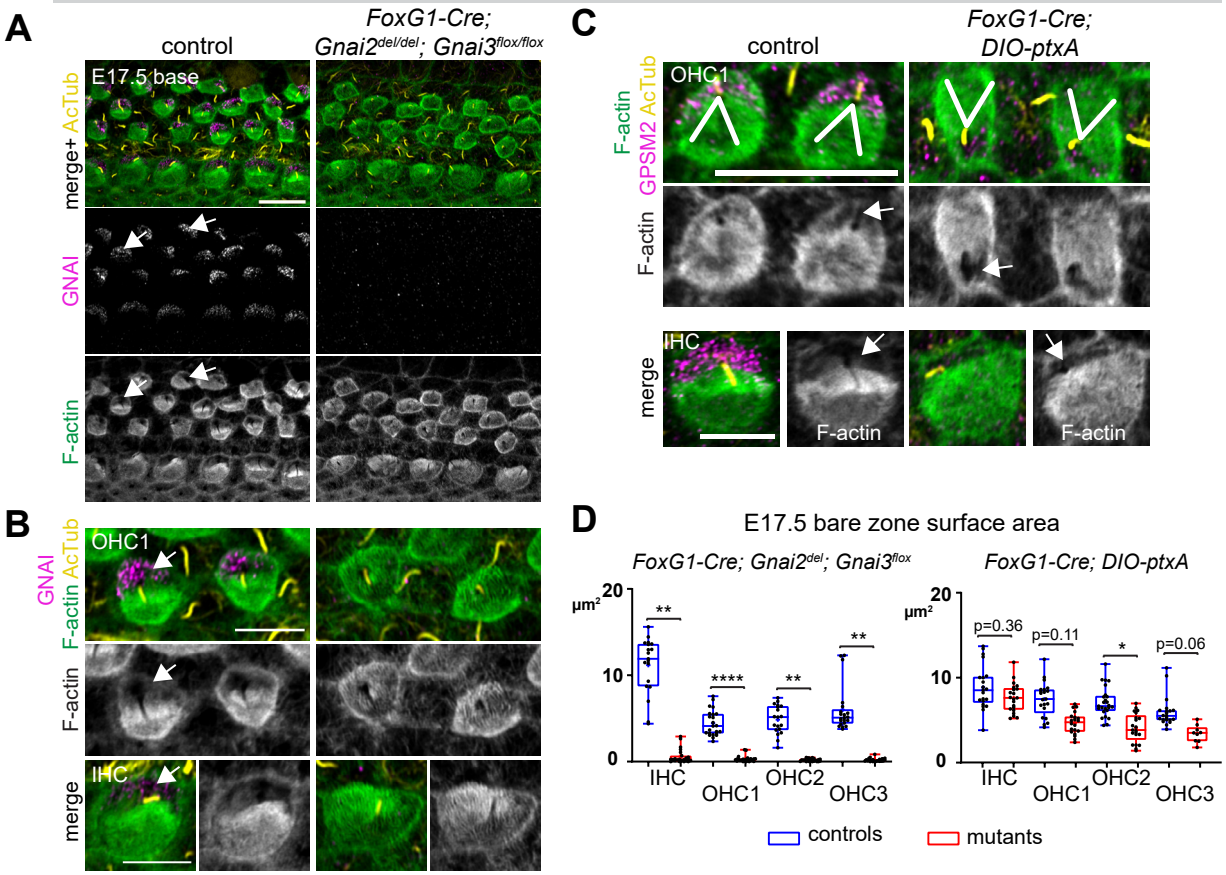
A
control
FoxG1-Cre; Gnai2del/del; Gnai3flox/flox
E17.5 base
merge+ AcTub
GNAI
F-actin
B
GNAI AcTub F-actin
OHC1
F-actin
merge
IHC
C
control
FoxG1-Cre; DIO-ptxA
OHC1
F-actin GPSM2 AcTub
F-actin
merge
IHC
F-actin
D
E17.5 bare zone surface area
FoxG1-Cre; Gnai2del; Gnai3flox
FoxG1-Cre; DIO-ptxA
µm²
IHC OHC1 OHC2 OHC3
p=0.36 p=0.11 p=0.06
controls
mutants

## P0

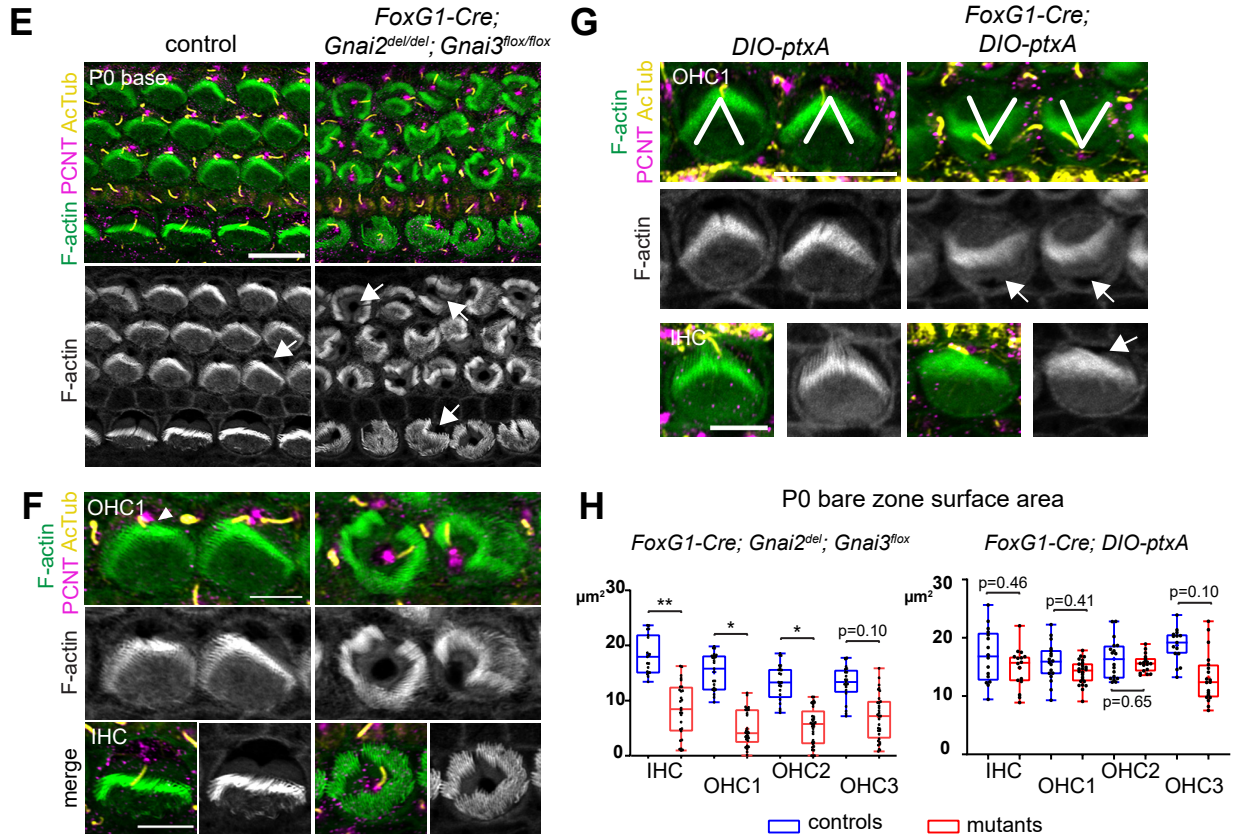
E
control
FoxG1-Cre; Gnai2del/del; Gnai3flox/flox
P0 base
F-actin PCNT AcTub
F-actin
F
OHC1
F-actin PCNT AcTub
F-actin
merge
IHC
G
DIO-ptxA
FoxG1-Cre; DIO-ptxA
OHC1
F-actin PCNT AcTub
F-actin
IHC
H
P0 bare zone surface area
FoxG1-Cre; Gnai2del; Gnai3flox
FoxG1-Cre; DIO-ptxA
µm²
IHC OHC1 OHC2 OHC3
p=0.10
p=0.46 p=0.41 p=0.65 p=0.10
controls
mutants

**Figure 6. Delayed bare zone expansion and severely dysmorphic hair bundles in absence of GNAI2 and GNAI3. A-B)** GNAI (scbt"GNAI3" antibody, see Fig. 4) and acetylated tubulin (AcTub; kinocilium) co-immunolabeling at the E17.5 cochlear base. Note how F-actin labeling (phalloidin) reveals a polarized bare zone marked by GNAI (arrows) in control but not in *Gnai2; Gnai3* double mutants. **C)** GPSM2 and AcTub co-immunolabeling at the E17.5 cochlear base. In contrast to *Gnai2; Gnai3* double mutants (A-B), *FoxG1-Cre; DIO-ptxA* mutants have a polarized bare zone (arrows) despite OHC1-2 adopting a reversed orientation (V brackets indicate OHC1 orientation). GPSM2 marks the bare zone in controls and is reduced in mutants. **D)** Graphs of bare zone surface area in E17.5 HC at the cochlear base. *FoxG1-Cre; Gnai2*$^{del}$*; Gnai3*$^{flox}$: controls (*Gnai2*$^{del/+}$*; Gnai3*$^{flox/+}$ and *Gnai2*$^{del/+}$*; Gnai3*$^{flox/flox}$) N=3 animals, n=19 IHC, 23 OHC1, 19 OHC2, 21 OHC3; mutants N=3, n=23 IHC, 24 OHC1, 23 OHC2, 24 OHC3. *FoxG1-Cre; DIO-ptxA*: controls (Cre-negative *DIO-ptxA*) N=3, n=18 IHC, 18 OHC1, 21 OHC2, 18 OHC3; mutants N=3, n= 21 IHC, 20 OHC1, 21 OHC2, 9 OHC3. **E-G)** Pericentrin (PCNT) and AcTub co-immunolabeling at P0 at the cochlear base. Unlike at E17.5 (A-B, D), most P0 *Gnai2; Gnai3* double mutant HC have a bare region (E-F, arrows). This bare region is unpolarized and its abnormal shape reflects aberrant stereocilia distribution. In sharp contrast, ptxA mutants have normally shaped hair bundles and bare zones despite OHC1-2 adopting a reversed orientation (G). **H)** Graphs of bare zone surface area in P0 HC at the cochlear base. *FoxG1-Cre; Gnai2*$^{del}$*; Gnai3*$^{flox}$: controls (*Gnai2*$^{del/+}$*; Gnai3*$^{flox/+}$, *Gnai2*$^{del/+}$*; Gnai3*$^{flox/flox}$ and *FoxG1-Cre; Gnai2*$^{del/+}$*; Gnai3*$^{flox/+}$) N=3, n=19 IHC, 23 OHC1, 21 OHC2, 21 OHC3; mutant N=3, n=21 IHC, 22 OHC1, 24 OHC2, 24 OHC3. *FoxG1-Cre; DIO-ptxA:* controls (Cre-negative *DIO-ptxA*) N=3, n=15 IHC, 23 OHC1, 18 OHC2, 15 OHC3; mutants N=3, n= 16 IHC, 24 OHC1, 18 OHC2, 19 OHC3. D, H: Nested (hierarchical) t-test sorted by animal; $p<0.01$ **, $p<0.05$ *; non-significant p-values are indicated. All *ptxA* samples are heterozygotes (*R26*$^{DIO\text{-}ptxA/+}$). Scale bars are 10μm (A, C (OHC), E, G (OHC)) and 5μm (B, C (IHC), F, G (IHC)).

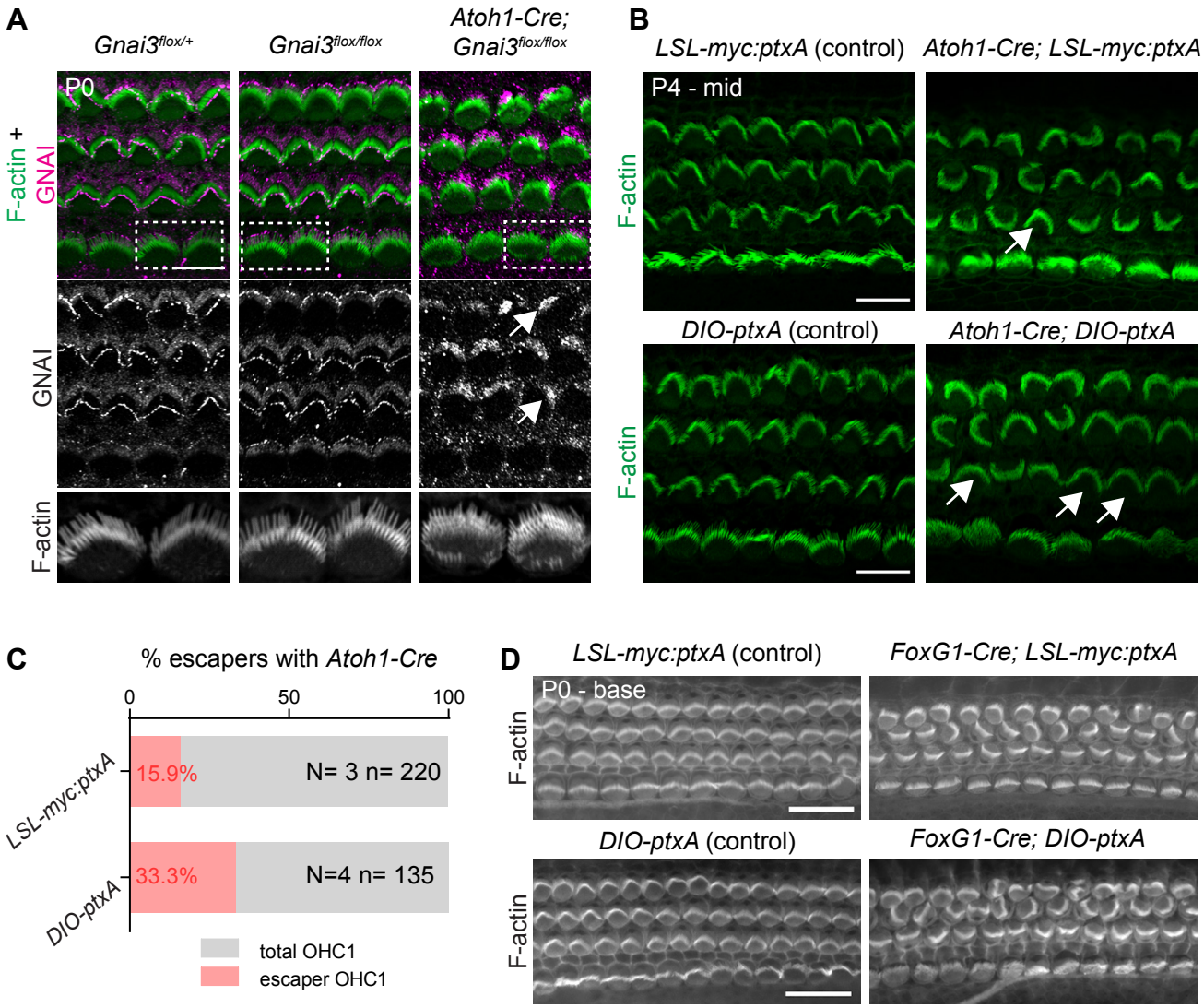


**Figure 6 Supplement 1. Validation of the *Gnai3*$^{flox}$ and *DIO-ptxA* mouse strains. A)** GNAI (pt"GNAI2" antibody; see Fig. 4) immunolabeling at the P0 cochlear base. Note how in absence of Cre recombinase, *Gnai3*$^{flox/flox}$ HC have normal hair bundles and normal GNAI enrichment at the bare zone and stereocilia tips. In contrast, *Atoh1-Cre* produces incomplete GNAI enrichment (arrows; compare with Fig. 4D) and shortened stereocilia typical of constitutive *Gnai3* mutants. Boxed IHC regions are magnified below. **B-D)** Comparison of the two *ptxA* strains used in this study (see also Fig. 2 Supp. 1C-D). PtxA expression with the *Atoh1-Cre* driver produces comparable P4 apical HC defects in the *LSL-myc:ptxA* and *DIO-ptxA* strains (B). "Escaper" OHC1 that are not inverted in orientation (arrows) likely do not express Cre, or did not undergo recombination. **C)** When *Atoh1-Cre* induces ptxA expression in post-mitotic HC, the number of escaper OHC1 is higher in the *DIO-ptxA* strain. This is likely because *lox*-based genomic deletions (LSL) are favored over genomic inversions (DIO; see Fig. 2 Supp. 1C-D). **D)** In contrast to *Atoh1-Cre*, an earlier Cre driver (*FoxG1-Cre)* shows virtually no escapers in either ptxA strain. N and n indicate the number of animals and OHC1 analyzed, respectively. All *ptxA* samples in the study are heterozygotes (*R26*$^{LSL\text{-}myc:ptxA/+}$ or *R26*$^{DIO\text{-}ptxA/+}$), and controls are Cre-negative heterozygotes. Scale bars are 10μm (A, B), 20μm (D).

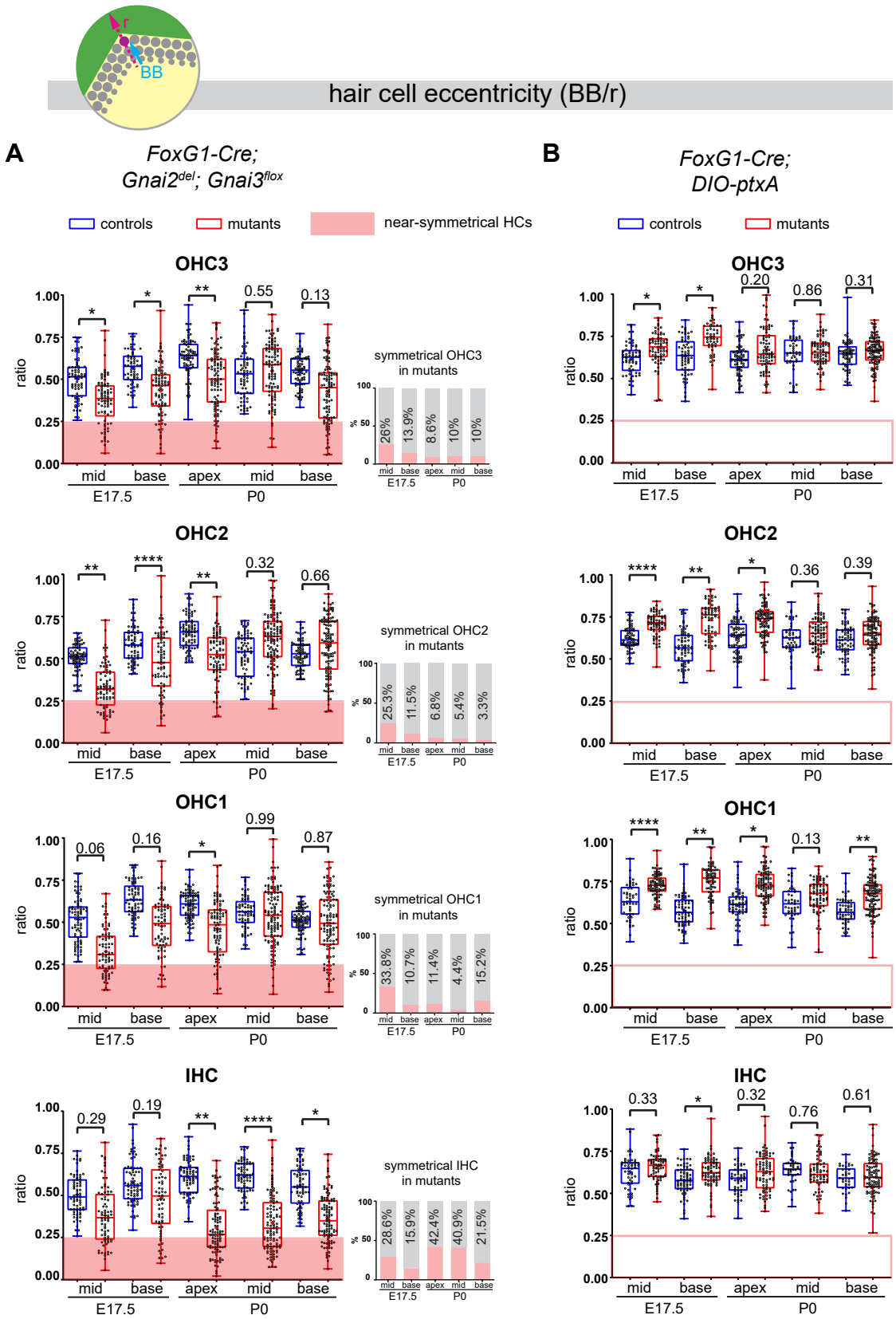


**Figure 7. Loss of GNAI2 and GNAI3 provokes hair cell eccentricity defects absent in *ptxA* mutants. A-B)** Graphs of HC eccentricity representing the position of the basal body as a ratio of the radius (BB/r, top diagram). Data cover E17.5 mid and base and P0 apex, mid and base cochlear positions for each HC type. HC were considered near-symmetrical when their eccentricity ratio was lower than 0.25 (red zone). Only *FoxG1-Cre; Gnai2*$^{del}$*; Gnai3*$^{flox}$ mutants harbor symmetrical HC. Their

proportion is indicated in the bar graphs on the right (A). Overall, the proportion of symmetrical cells tends to decrease in maturing OHC but remains high or increases in IHC. At least 3 animals and 39 cells per HC type are represented for each stage, cochlear position and genotype (detailed in Source Data file). Controls for *FoxG1-Cre; Gnai2*$^{del/del}$*; Gnai3*$^{flox/flox}$ are *Gnai2*$^{del/+}$*; Gnai3*$^{flox/+}$, *Gnai2*$^{del/+}$*; Gnai3*$^{flox/flox}$, *FoxG1-Cre; Gnai2*$^{del/+}$*; Gnai3*$^{flox/+}$ and *FoxG1-Cre; Gnai2*$^{del/+}$*; Gnai3*$^{flox/flox}$. Controls for *FoxG1-Cre; DIO-ptxA* are Cre-negative *DIO-ptxA* heterozygotes. Nested (hierarchical) t-test sorted by animal; $p<0.0001$ ****, $p<0.01$ **, $p<0.05$ *; non-significant p-values are indicated. Detailed cohort sizes and statistics can be found in Source Data file.

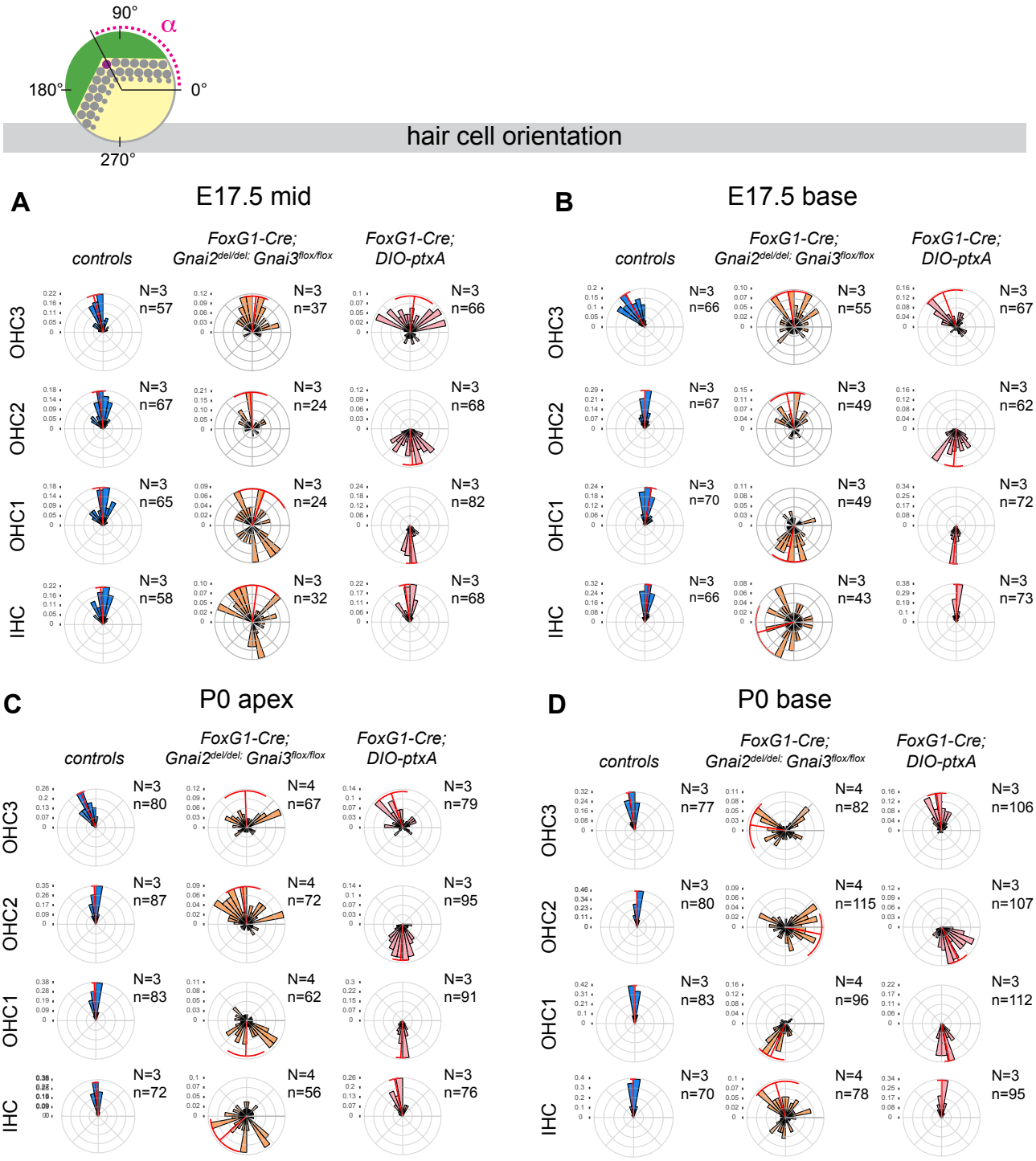


**Figure 8. Loss of GNAI2 and GNAI3 recapitulates hair cell orientation defects observed in *ptxA* mutants. A-D)** Circular histograms showing HC orientation (α) based on the position of the basal body (purple dot in top diagram) at the stage and cochlear position indicated. 0° is towards the cochlear base and 90° is lateral. HC represented have an eccentricity greater than 0.4 in A-B (E17.5), and 0.25 in C-D (P0) (see Fig. 7). Histograms show frequency distribution (10° bins) and red radial lines and arcs respectively indicate circular mean and circular mean deviation. In control cochleae, HC are tightly oriented laterally (90°) except for OHC3 that show a slight bias towards the cochlear apex (180°). As reported previously, ptxA expression inverts OHC1 and OHC2, and results in imprecise lateral orientation of OHC3. This phenotype is recapitulated in *Gnai2; Gnai3* double mutants with a

delay (compare least mature E17.5 mid (A) and most mature P0 base (D)). IHC also show severe misorientation in *Gnai2; Gnai3* double mutants, unlike in *ptxA* mutants. n, HC number in N=3-4 animals. Controls for *FoxG1-Cre; Gnai2*$^{del/del}$*; Gnai3*$^{flox/flox}$ are *Gnai2*$^{del/+}$*; Gnai3*$^{flox/+}$, *Gnai2*$^{del/+}$*; Gnai3*$^{flox/flox}$, *FoxG1-Cre; Gnai2*$^{del/+}$*; Gnai3*$^{flox/+}$ and *FoxG1-Cre; Gnai2*$^{del/+}$*; Gnai3*$^{flox/flox}$. Data at the P0 cochlear mid position can be found in Fig. 8 Supp. 1A. Histograms for littermate controls of *FoxG1-Cre; DIO-ptxA* mutants can be found in Fig. 8 Supp. 2. Detailed cohorts and results can be found in Source Data file.

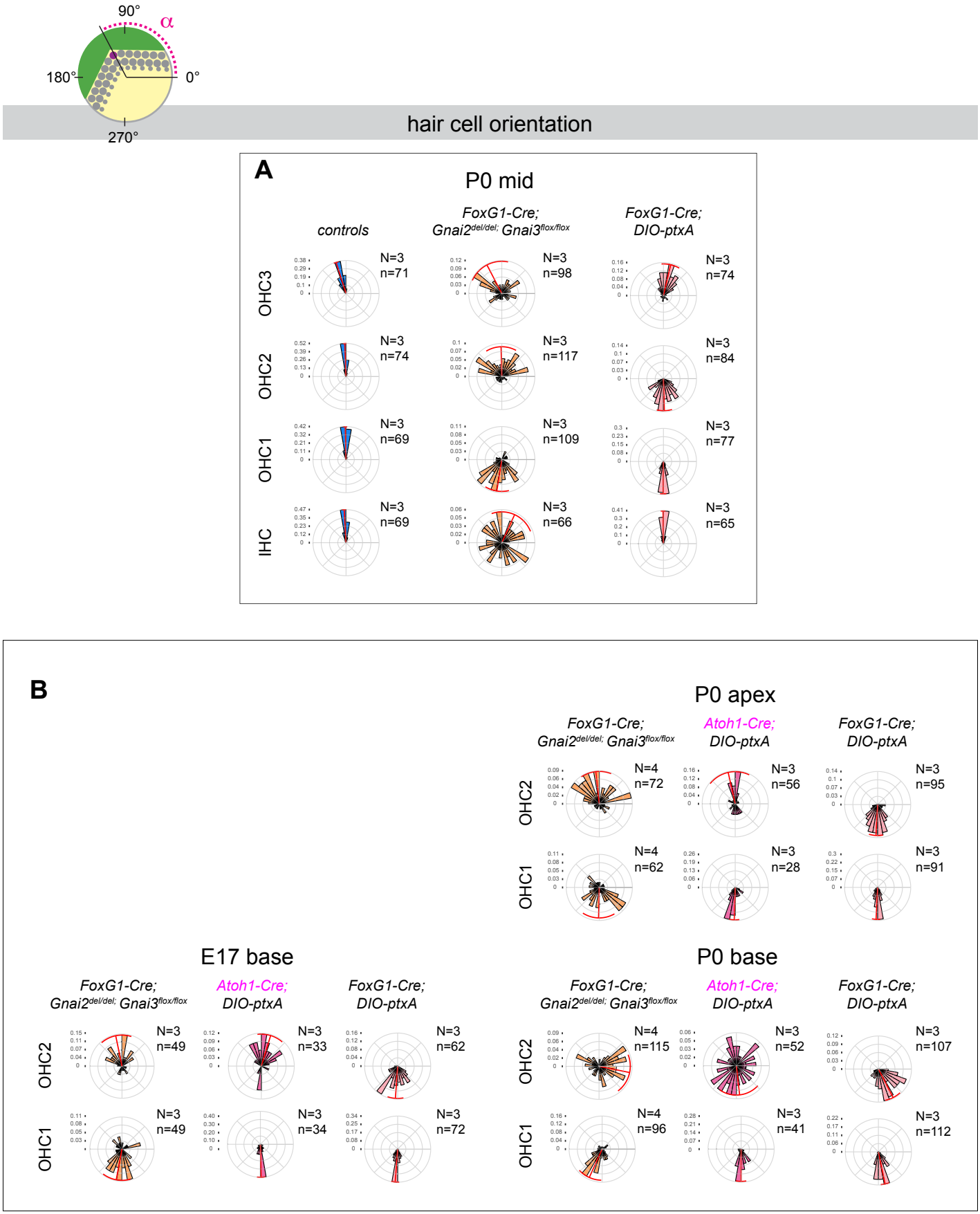


**Figure 8 Supplement 1. Loss of GNAI2 and GNAI3 recapitulates hair cell orientation defects observed in *ptxA* mutants. A)** P0 mid-cochlea histograms that complement P0 apex and P0 base histograms in Fig. 8C-D. **B)** Comparison of OHC1 and OHC2 orientation in *FoxG1-Cre; Gnai2*$^{del/del}$*;*

*Gnai3*$^{flox/flox}$ (left diagrams; identical to Fig. 8A, C-D), *Atoh1-Cre; DIO-ptxA* (center diagrams) and *FoxG1-Cre; DIO-ptxA* mutants (right diagrams; identical to Fig. 8A, C-D) at the E17.5 base, P0 apex and P0 base. Post-mitotic Cre expression in *Atoh1-Cre* HC results in delayed *ptxA* expression and delayed inversion of OHC2 compared to earlier *FoxG1-Cre* expression in progenitor cells. This outcome is reminiscent of *Gnai2; Gnai3* mutants. At the E17.5 base and P0 apex (less mature), most OHC2s are inverted in the *FoxG1-Cre; DIO-ptxA* model only. At the P0 cochlear base (more mature), OHC2s are largely inverted in *Gnai2; Gnai3* mutants and in the *Atoh1-Cre; DIO-ptxA* model as well. Circular histograms show HC orientation ($\alpha$) based on the position of the basal body (purple dot in top diagram) at the stage and cochlear position indicated. 0° is towards the cochlear base and 90° is lateral/abneural. HC represented have an eccentricity greater than 0.4 (E17.5) or 0.25 (P0) . Histograms show frequency distribution (10° bins) and red radial lines and arcs respectively indicate the circular mean and the circular mean deviation. n, HC number in N=3-4 animals. Littermate control histograms for *Atoh1-Cre; DIO-ptxA* mutants (B) can be found in Fig. 8 Supp. 2F.

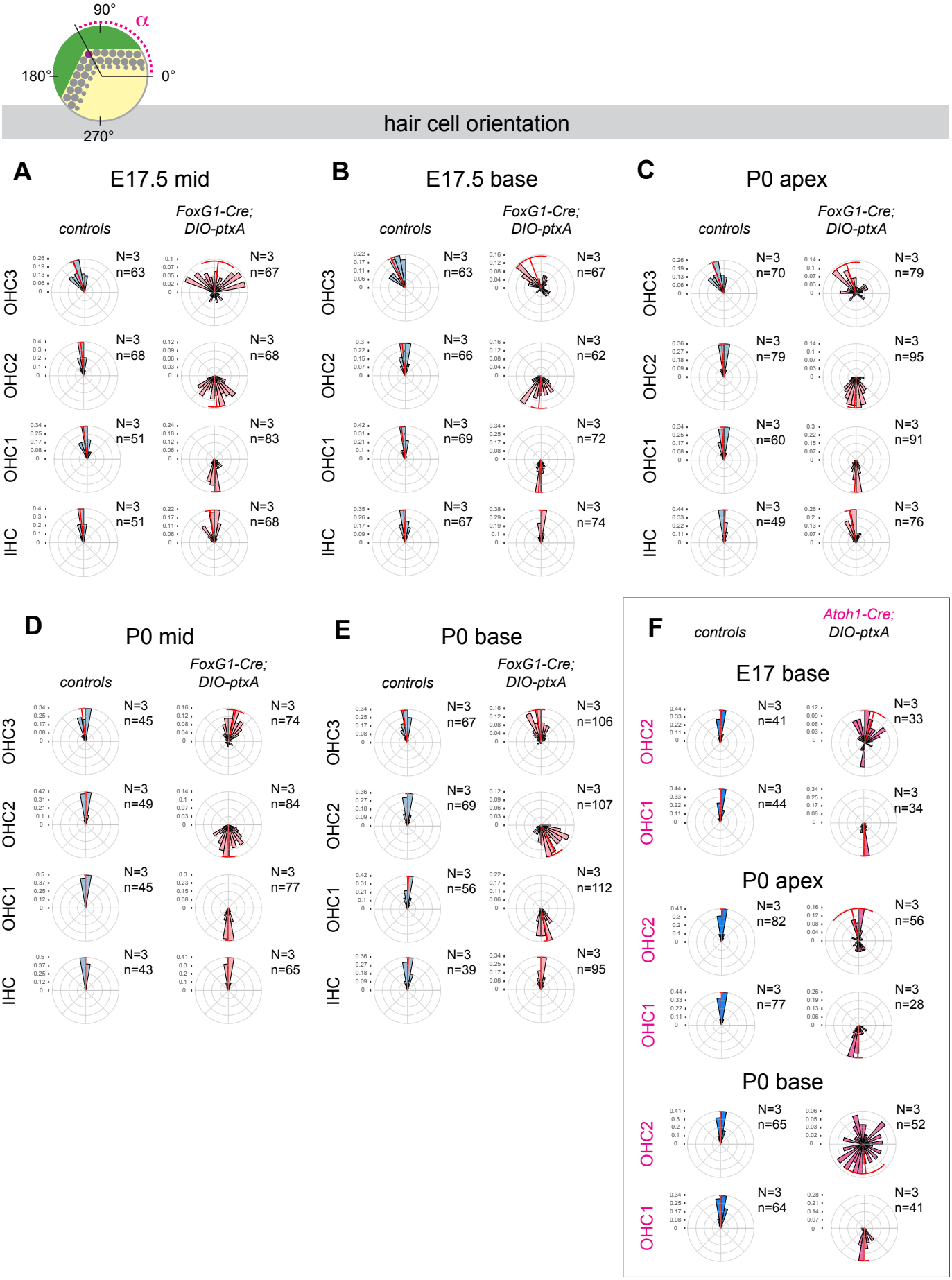
90°
α
180°
0°
270°
hair cell orientation
A
E17.5 mid
controls
FoxG1-Cre; DIO-ptxA
OHC3
OHC2
OHC1
IHC
N=3 n=63
N=3 n=67
N=3 n=68
N=3 n=68
N=3 n=51
N=3 n=83
N=3 n=51
N=3 n=68
B
E17.5 base
N=3 n=63
N=3 n=67
N=3 n=66
N=3 n=62
N=3 n=69
N=3 n=72
N=3 n=67
N=3 n=74
C
P0 apex
N=3 n=70
N=3 n=79
N=3 n=79
N=3 n=95
N=3 n=60
N=3 n=91
N=3 n=49
N=3 n=76
D
P0 mid
N=3 n=45
N=3 n=74
N=3 n=49
N=3 n=84
N=3 n=45
N=3 n=77
N=3 n=43
N=3 n=65
E
P0 base
N=3 n=67
N=3 n=106
N=3 n=69
N=3 n=107
N=3 n=56
N=3 n=112
N=3 n=39
N=3 n=95
F
controls
Atoh1-Cre; DIO-ptxA
E17 base
OHC2
OHC1
N=3 n=41
N=3 n=33
N=3 n=44
N=3 n=34
P0 apex
N=3 n=82
N=3 n=56
N=3 n=77
N=3 n=28
P0 base
N=3 n=65
N=3 n=52
N=3 n=64
N=3 n=41

**Figure 8 Supplement 2. Littermate control histograms for *ptxA* mutants. A-E)** Histograms showing littermate controls for *FoxG1-Cre; DIO-ptxA* mutants in Fig. 8 (A-C, E) and in Fig. 8 Supp. 1A (D; P0 mid), and littermate controls for *Atoh1-Cre; DIO-ptxA* mutants in Fig. 8 Supp. 1B (F). Note that mutant histograms are identical to Fig. 8 or Fig. 8 Supp. 1. Circular histograms show HC orientation ($\alpha$) based on the position of the basal body (purple dot in top diagram) at the stage and cochlear position indicated. 0° is towards the cochlear base and 90° is lateral/abneural. HC represented have an eccentricity above 0.4 at E17.5 and above 0.25 at P0. Histograms show frequency distribution (10° bins) and red radial lines and arcs respectively indicate the circular mean and the circular mean deviation. n, HC number in N=3-4 animals. Controls for *FoxG1-Cre; DIO-ptxA* and *Atoh1-Cre; DIO-ptxA* are Cre-negative *DIO-ptxA* heterozygotes. Detailed cohorts and results can be found in Source Data file.

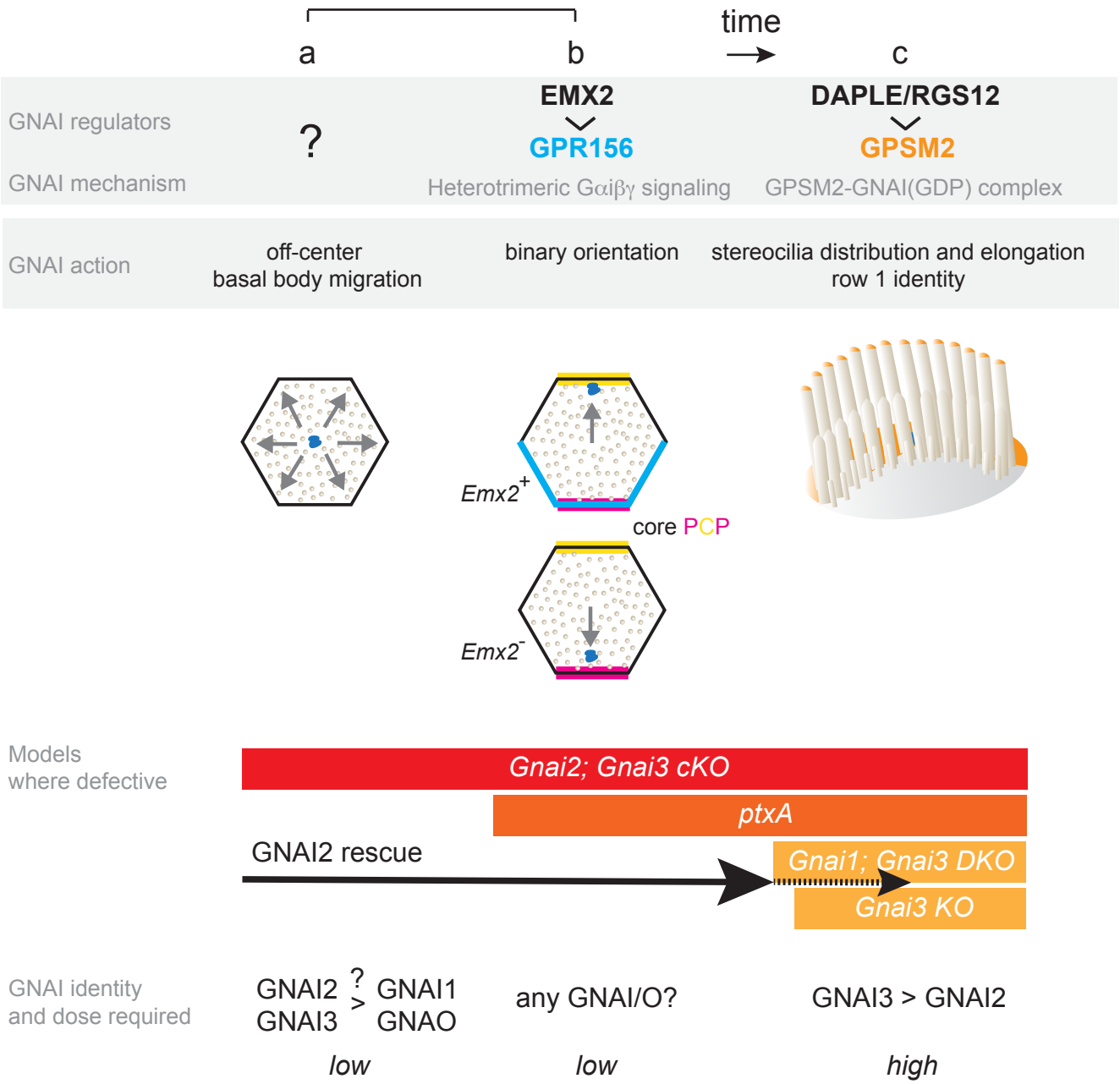


**Figure 9. Summary and model: three roles validated *in vivo* for GNAI proteins during hair cell polarized morphogenesis.** GNAI proteins are required for the off-center migration of the basal body, and thus HC symmetry breaking (a). This activity is distinct from defining binary HC orientation downstream of GPR156 (b), as *Gpr156* mutant HC have off-center basal bodies and normal hair bundles. Finally, GNAI partner with GPSM2 to shape the hair bundle and elongate stereocilia (c). The specific identity and the dosage of GNAI proteins required differ for each role. GNAI3 is the principal architect of hair bundle development (c), with GNAI2 plays an important but progressively waning role. High amounts of GNAI3/GNAI2 are required with GPSM2. A lower dose of GNAI/O proteins is required for embryonic role, and we speculate that GNAI2 and GNAI3 play a prominent role for symmetry-breaking (a) whereas any GNAI/O protein may effectively signal downstream of GPR156 for proper HC orientation (b). A GNAI/O regulator for symmetry breaking remains to be identified.

| Gene or model | Official name | Name in the study | MGI # | Reference | Allele description | Genetic background | Genetic background in the study | % surviving mutants at weaning age | |
|---|---|---|---|---|---|---|---|---|---|
| ***Gnai1*** | *Gnai1* $^{tm1Lbi}$ | *Gnai1* $^{neo}$ | | Jiang et al, 2002 PMID: 36092739 | neo cassette inserted in exon 3 | | 129S1/SvImJ: C57BL/6J mix | *from het x het (expected 25%)* 16.4% (12 of 73 animals) | *from hom x het (expected 50%)* 45.8% (49 of 107 animals) |
| ***Gnai2*** | *Gnai2* $^{em1Btar}$ | *Gnai2* $^{del}$ | | this study | CRISPR/Cas9 deletion of exons 2-3-4 | C57BL/6J | C57BL/6J | 9.9% (15 of 152 animals) | 9.6% (5 of 52 animals) |
| | | | | | | | C57BL/6J: FVB/NJ mix | 19.7% (12 of 61 animals) | 46.7% (50 of 107 animals) |
| ***Gnai3*** | *Gnai3* $^{tm1Lbi}$ | *Gnai3* $^{neo}$ | | Jiang et al, 2002 PMID: 36092739 | part of intron 5 and exon 6 replaced with a neo cassette | | 129S1/SvImJ: C57BL/6J mix | 30% (12 of 40 animals) | 42% (63 of 150 animals) |
| | | *Gnai3* $^{flox}$ | | this study | floxed exons 2-3 | C57BL/6J | C57BL/6J | | |
| ***Gnao1*** | *Gnao1* $^{tm1Lbi}$ | *Gnao1* $^{neo}$ | 2152685 | Jiang et al, 1998 PMID: 9501252 | neo cassette inserted in exon 6 | 129S1/SvImJ | 129S1/SvImJ | *from het x het (expected 25%)* 6.7% (3 animals out of 45) | |
| | *Gnao1* $^{tm1c(EUCOMM)Hmgu}$ | *Gnao1* $^{flox}$ | from 4456727 | KOMP | floxed exon 3 - derived from Gnao1tm1a(EUCOMM)Hmgu via FLP-based removal of LacZneo cassette | C57BL/6N | C57BL/6N | *from Atoh1-Cre; het x het (expected 12.5% cKO)* 40% (10 *Atoh1-Cre; flox* hom of 25 animals) | *from Atoh1-Cre; hom x het (expected 25% cKO)* 30.7% (4 *Atoh1-Cre; flox* hom of 13 animals) |
| ***Gnai1; Gnai2*** | *Gnai1* $^{tm1Lbi}$ *; Gnai2* $^{em1Btar}$ | *Gnai1* $^{neo}$ *; Gnai2* $^{del}$ | | Jiang et al, 2002 PMID: 36092739; this study | | | 129S1/SvImJ: C57BL/6J:FVB/NJ mix | *from het; het x het; het (expected 6.25%)* 5,8% (7 of 121 animals) | *from hom; het x hom; het (expected 25% dKO)* 6.9% (2 of 29 animals) |
| ***Gnai1; Gnai3*** | *Gnai1* $^{tm1Lbi}$ *; Gnai3* $^{tm1Lbi}$ | *Gnai1* $^{neo}$ *; Gnai3* $^{neo}$ | 5560183 | Jiang et al, 2002 PMID: 36092739 | | 129S1/SvImJ | 129S1/SvImJ | *from hom; het x hom; het (expected 25% dKO)* 22.2% (20 of 90 animals) | *from hom; hom x hom; het (expected 50% dKO)* 43.2% (60 of 137 animals) |
| ***FoxG1-Cre; Gnai2; Gnai3*** | | *Gnai2* $^{del}$ *; Gnai3* $^{flox}$ | | this study | | | 129S1/SvImJ: C57BL/6J:FVB/NJ mix | *second generation crosses* 0% (0 out of 149 animals) | *first generation crosses* 0.3% (1 out of 333 animals) |
| ***ptxA*** | *Gt(ROSA)26Sor* $^{tm1(ptxA)Cgh}$ | *LSL-ptxA:myc* | 3776029 | Regard et al, 2007 PMID: 17992256 | *loxP-stop-loxP* cassette before *ptxA:myc* | C57BL/6:129SvJ | | | |
| | *Gt(ROSA)26Sor* $^{em1(ptxA)Btar}$ | *LSL-myc:ptxA* | 6163665 | Tarchini et al, 2016 PMID: 27660326 | *loxP-stop-loxP* cassette before *myc:ptxA* | C57BL/6J | C57BL/6J | | |
| | | *DIO-ptxA* | | this study | double inverted *lox* sites flanking *ptxA* | C57BL/6J | C57BL/6J | | |
| ***Atoh1-Cre*** | *Tg(Atoh1-cre)1Bfri* | *Atoh1-Cre* | 3775845 | Matei et al, 2005 PMID: 16145671 | randomly inserted transgene with *Atoh1* enhancer | (C57BL/6 x CBA)F1 | C57BL/6 | | |
| ***FoxG1-Cre*** | *Foxg* $^{1tm1(cre)Skm}$ | *FoxG1-Cre* | 1932522 | Hebert et al, 2000 PMID: 10837119 | Cre knock-in in the *FoxG1* gene | 129P2/OlaHsd-Hprtb-m3 | 129S1/SvImJ: C57BL/6J mix | | |

**Supplementary Table 1. Mouse strain details.**

| Strain | | Primer sequence | Bands size (bp) | |
|---|---|---|---|---|
| *Gnao1* $^{flox}$ | forward | 5' - TGGGTTTGATCCACAAGAGCGG - 3' | | |
| | forward | 5' - AGACGTGAAGCAGTACAAGC - 3' | | |
| | reverse | 5' - TCTCCTCAGTAGGGAAGATGGC - 3' | | |
| | | | wt: 938; flox: 1119 | wt: 387; flox: 421 |
| *Gnao1* $^{neo}$ | forward | 5' - TGGTGACCCATTCTGACTTC - 3' | | |
| | forward | 5' - TCGCCTTCTATCGCCTTCTTGACG - 3' | | |
| | reverse | 5' - TTGGCAGAGAAAGCCCAAAG - 3' | | |
| | | | wt: 836 | neo: 461 |
| *Gnai1* $^{neo}$ | forward | 5' - TCTAGGTGCTGGGGAATCTG - 3' | | |
| | reverse | 5' - GAGACGTGCTACTTCCATTTGTC - 3' | | |
| | reverse | 5' - TGAGCTTGTAGGCACAGAGG - 3' | | |
| | | | wt: 1004 | neo: 580 |
| *Gnai2* $^{del}$ | forward | 5' -GCACCATCGTCAAGCAGATG - 3' | | |
| | forward | 5' - ATGGGTGGTTGTGAGCCATC - 3' | | |
| | reverse | 5' - GAGCTGGTATTCTCGTGAGC - 3' | | |
| | | | wt: 728 | wt: 1195; neo: 515 |
| *Gnai3* $^{neo}$ | forward | 5' - CTTCTATCGCCTTCTTGACG - 3' | | |
| | forward | 5' -ACTCTGCTGACTTTGGCACC - 3' | | |
| | reverse | 5' - CTTTCATGCATTCGGTTCTG - 3' | | |
| | | | wt: 762 | neo: 450 |
| *Gnai3* $^{flox}$ | forward | 5' - ATGAGGACGGCTATTCAGAG - 3' | | |
| | reverse | 5' - CATCCTACTTCACAAACTGC - 3' | | XhoI digestion |
| | | | wt: 700; flox: 747 | wt: 700; flox: 342 + 404 |
| *LSL-myc:ptxA* | forward | 5' - AAAGTCGCTCTGAGTTGTTAT - 3' | | |
| | reverse | 5' - GCGAAGAGTTTGTCCTCAACC - 3' | | |
| | reverse | 5' - GGAGCGGGAGAAATGGATATG - 3' | | |
| | | | wt: 603 | ptxA: 250 |
| *DIO-ptxA* | forward | 5' - GCACTTGCTCTCCCAAAGTC - 3' | | |
| | reverse | 5' - GGAGCGGGAGAAATGGATATG - 3' | | |
| | reverse | 5' - CGTCATTGACGTCAATAGGG - 3' | | |
| | | | wt: 617 | ptxA: 677 |
| *Atoh1-Cre* | forward | 5' - AGAGCGGCTGACAATAGAGG - 3' | | |
| | reverse | 5' - TTTCCATGAGTGAACGAACC - 3' | | |
| | | | wt: no band | cre: 850 |
| *FoxG1-Cre* | forward | 5' - GCGACAAGAAGAACGGCAAG - 3' | | |
| | forward | 5' - GCAAGAACCTGATGGACATG - 3' | | |
| | reverse | 5' - AAGCACTTGTTGAGGGACAG - 3' | | |
| | reverse | 5' - TTTCCATGAGTGAACGAACC - 3' | | |
| | | | wt: 202 | cre: 381 |

**Supplementary Table 2. Genotyping strategies.**